Growth-dependent sensory bet-hedging enhances collective navigation

Fotios Avgidis[1,2,3], Ruta Jurgelyte[1], Thierry Emonet[2,3,4*], Thomas S. Shimizu[1*]

[1]Center for Living Systems, AMOLF Institute, Amsterdam, 1098 XG, The Netherlands.
[2]Department of Molecular, Cellular, and Developmental Biology, Yale University, New Haven, 06511, CT, USA.
[3]Quantitative Biology Institute, Yale University, New Haven, 06511, CT, USA.
[4]Department of Physics, Yale University, New Haven, 06511, CT, USA.

*Corresponding author(s). E-mail(s): thierry.emonet@yale.edu; shimizu@amolf.nl;

Abstract

Phenotypic heterogeneity in microbes can be a double-edged sword — boosting individual survival in uncertain environments, but potentially compromising beneficial population coordination. Dissecting how microbes resolve this tradeoff is challenging because interactions span multiple scales—from molecular interactions to single-cell behavior, population dynamics, and environmental feedback. Here, we address this question for the *Escherichia coli* chemotaxis system, which implements both individual motile explorations and collective resource exploitations using the same cellular machinery. We quantify the heterogeneity of individual sensory and behavioral phenotypes, as well as the abundance of key signaling proteins during growth in various environments, and test their impact on population-scale collective migration. We identify growth rate as a key environment-dependent physiological variable governing not only the mean but also the variance of sensory phenotypes. Remarkably, rather than hindering population coordination, we find that sensory diversity benefits collective chemotactic navigation in uncertain environments. Strong heterogeneity of expressed phenotypes enhances readiness to multiple sensory cues, and the required population coordination is achieved by phenotypic filtering of that diversity by the collective behavior itself. These results reveal a sensory bet-hedging strategy for collective navigation during population growth: diversity in sensitivity to nutrients currently being consumed is reduced to promote focused exploitation, while it is increased for nutrients not yet encountered to enhance exploration for new growth opportunities.

1 Introduction

The survival of an organism depends upon its capacity to adeptly perceive and respond to environmental cues, such as nutrient resources required for growth. This faculty is particularly important for microbes such as bacteria, which inhabit diverse ecosystems characterized by rapid and unpredictable changes, such as terrestrial soils or the mammalian gut [1]. Growing populations are often confronted with exhaustion of a particular nutrient source, as well as new encounters with alternative resources. A strategy to cope with such unpredictability is to establish a population that mixes individuals of different phenotypes. This diversification, often called "bet-hedging", can enhance collective readiness of populations to a range of environmental changes, by maintaining subpopulations of individuals prepared for contrasting future scenarios [2–8].

Yet phenotypic diversity also poses challenges for population-level coordination. Many collective microbial processes such as quorum sensing [9, 10], biofilm formation [11, 12], and antibiotic defense [13, 14] depend on secreted signals or public goods reaching some threshold, and can fail if the fraction of non-secreting (or "cheater") cells is too high. Microbial developmental programs such as sporulation waves in B. subtilis [15, 16] and fruiting body formation in M. xanthus [17, 18], as well as host manipulation and invasion strategies by pathogens [19, 20] tend to require synchronized state transitions across the population. And in chemotactic bacteria, efficient collective exploitation of nutrient resources requires traveling-wave range expansion by populations with matched chemotactic velocities [21–23]. In all of these cases, nonzero diversity tends to confer bet-hedging advantages (cells that do not to invest in the collective phenotype often are endowed with reproductive or survival advantages), but excessive phenotypic heterogeneity clearly becomes detrimental.

What are the strategies and mechanisms by which microbial populations negotiate this tension? In this study, we address this question in the *Escherichia coli* chemotaxis system, which controls motile navigation both at the level of individual cells by biasing a run-and-tumble random walk, and at the level of the population, by generating chemotactic population waves that migrate at a constant speed. Previous work established that the chemosensory system controlling this motile behavior exhibits phenotypic diversity suggestive of bet-hedging [24–30], and that it can rapidly modulate its phenotype distribution without changes in gene expression through a diversity-tuning mechanism based on covalent modification of allosterically interacting chemoreceptors [8, 31]. However, that posttranslational mechanism works by effectively filtering the underlying diversity in protein counts, which can itself vary on a slower timescale due to stochastic gene expression. We therefore began by characterizing single-cell sensory phenotypes and stochastic gene expression under various environmental conditions, before examining their implications for collective navigation performance.

At the single-cell level, *E. coli* moves through space by a run-and-tumble random walk [32]. To bias this random walk towards attractants and away from repellents, *E. coli* makes use of the chemotaxis pathway, one of the best characterized models of biological signaling. *E. coli* cells detect chemical and physical signals through arrays of transmembrane receptors composed of five different types of chemoreceptors. The two primary receptors, Tar (which mainly senses the amino acid aspartate) and Tsr (which mainly senses the amino acid serine), make up 90% of the total chemoreceptor population when *E. coli* cells are grown in rich media. The other three chemoreceptors—Tap, Trg, and Aer—are present at substantially lower copy numbers [33]. The receptors modulate the activity of the kinase CheA, which phosphorylates the response regulator CheY, producing CheY-P. Binding of attractant molecules to chemoreceptors reduces the activity of CheA, leading to a decrease in the intracellular level of CheY-P due to the activity of the phosphatase CheZ. CheY-P interacts with the flagellar motor, reducing the bacterium's tendency to tumble. Consequently, attractant binding increases the duration of the bacterium's runs, biasing the random walk in the desired direction.

We characterized the diversity of *E. coli*'s sensory and motility phenotypes, as well as the expression of its two major chemoreceptors, Tar and Tsr, under various growth conditions. Specifically, by combining the single-cell FRET microscopy method developed in our lab [27] with a microfluidic device that allows tracking hundreds of swimming trajectories simultaneously [34] and fluorescent fusions of Tar and Tsr, we quantified sensory and behavioral diversity alongside gene expression noise in isogenic bacteria under nutrient-rich and nutrient-poor environments. Our findings reveal that changes in nutrient composition and cell density alter not only the average sensory phenotype but also the degree of cell-to-cell variability in sensory responses. In contrast, motility phenotypes —specifically the tumble bias and run speed, which together define the run-and-tumble random walk in the absence of a chemical gradient — remain constant across all tested environments.

By combining experiments and mathematical analysis of a multi-species allosteric (MWC) model [35, 36], we demonstrate that the standing level of sensory diversity can be explained by changes in just one cellular random variable governed by stochastic gene expression: the Tar/Tsr receptor protein ratio.

By utilizing custom microfluidic chemostats amenable to single-cell fluorescence microscopy (variants of the "mother machine" [37]), we found that the chemical composition of the growth environment, rather than growth duration, dictates the distribution of the Tar/Tsr ratio through a growth rate-dependent gene expression mechanism.

Finally, by generating populations of cells with increased diversity in sensory phenotypes, we show that a high level of standing diversity confers a discernible advantage for chemotactic navigation under behavioral contexts where populations are challenged with different chemoattractants as environmental sensory cues. This advantage arises from the rapid filtering for the best-performing phenotypes by the collectively migrating chemotactic population wave, and occurs independently of gene expression changes — a novel population-level adaptation mechanism we recently predicted and verified experimentally [34, 38].

The gene-expression-based diversity adaptation mechanism we describe here operates on a timescale of hours, acting in parallel with the faster, non-genetic collective migration adaptation mechanism that occurs within minutes, and the posttranslational diversity tuning mechanism which operates on the sensory adaptation timescale of ~ 10 seconds.

2 Results

2.1 Single-cell FRET reveals substantial diversity in ligand sensitivity across an isogenic population of cells

To probe the degree of cell-to-cell variation in ligand sensing within a genetically identical population, we performed dose-response measurements by stimulating *E. coli* cells with pulses of the attractant amino acid L-serine that binds the major chemoreceptor Tsr, while monitoring the output of the signaling pathway in single cells using an *in vivo* CheYZ FRET sensor [27] for the activity of the kinase CheA (Figure 1a). *E. coli* has a sensory adaptation system consisting of the enzymes CheR and CheB that modulate the sensitivity of the chemoreceptors via covalent modifications that maintain the kinase output of the pathway to a constant steady-state level. To decouple diversity in ligand sensitivity from diversity in receptor modification induced by the two adaptation enzymes, we deleted the genes encoding CheR and CheB. We performed dose-response measurements (see methods) with cells grown as batch culture in nutrient-rich (TB) medium containing all 20 amino acids until mid-exponential phase, corresponding to an optical density (OD) of 0.45. The resulting dose-response data were fitted with a sigmoidal Hill function of the form $\frac{1}{1+\left(\frac{[L]}{K_{1/2}}\right)^H}$, where $\frac{1}{K_{1/2}}$, represents ligand sensitivity and H the cooperativity between receptors. This analysis revealed that single-cell dose-response curves can differ substantially from the population-average curve (Figure 1b). Extracting the $K_{1/2}$ parameter from these single-cell curves, which corresponds to the ligand concentration necessary to reduce the kinase activity by 50%, revealed a substantial degree of diversity, with the $K_{1/2}$ values of individual cells spanning approximately an order of magnitude (Figure 1b), consistent with our previous findings [8, 27, 31] .

2.2 Sensitivity distributions shift as a function of cell density in rich media, but not in minimal media

Considering that *E. coli* can be found in a variety of nutrient-diverse ecological niches, we wondered how chemosensory diversity is influenced by the growth environment. We cultured isogenic populations of cells in the same nutrient-rich batch culture and suspended growth by harvesting at four different cell densities, ranging from OD = 0.30 to OD = 0.80, where cells experience different nutrient concentrations [39–41]. Serine dose-response experiments revealed that the distribution of the inverse ligand sensitivity, $K_{1/2}$, shifts towards higher values with increasing cell density (Figure 1c). Notably, the diversity in $K_{1/2}$, measured as the coefficient of variation (CV, defined as standard deviation divided by the mean), increases considerably with cell density, ranging from CV = 0.20 at OD = 0.30 to CV = 0.45 at OD = 0.80.

We then examined how diversity varies as a function of cell density in an environment devoid of chemotactic cues. Cells were grown in minimal media without amino acids, using glycerol as a carbon source, which does not elicit a chemotactic response [42]. Compared to cells grown in rich media, these cells exhibited reduced sensitivity (higher $K_{1/2}$) in their responses to serine (Figure 1d). Notably, in minimal media, the distribution of $K_{1/2}$ remained independent of cell density, in contrast to the density-dependent shifts observed in rich media. Furthermore, the coefficient of variation of $K_{1/2}$ remained very high (CV ~ 0.50) across all cell densities in minimal media.

Finally, we wondered how the sensitivity to the other major *E. coli* chemoattractant, L-aspartate, which binds the chemoreceptor Tar, is modulated by the growth environment. We performed experiments identical to those described above, substituting serine with aspartate. Interestingly, in rich media, we observed the opposite trend compared to serine: cells exhibited higher sensitivity to aspartate (lower $K_{1/2}$) at higher cell densities (Figure 1e). However, as with serine, the distribution of aspartate $K_{1/2}$ was independent of cell density in minimal media (Figure 1f). We found that the coefficient of variation of aspartate $K_{1/2}$ was also notably high, ranging from CV = 0.91 at OD = 0.30 to CV = 0.34 at OD = 0.80. In minimal media, the CV of aspartate $K_{1/2}$ remained very high (CV $\sim$ 0.80) across all cell densities.

In summary, these results reveal an inverse scaling of serine and aspartate sensitivity with cell density in rich media: as cell density increases, sensitivity to aspartate increases (lower $K_{1/2}$), whereas sensitivity to serine decreases (higher $K_{1/2}$) (Figure 1g). In contrast, in minimal media, the sensitivities to both attractants are typically lower than in rich media and remain invariant with respect to cell density (Figure 1h).

2.3 Tar/Tsr ratio distribution shifts as a function of cell density in rich media, but not in minimal media

Next, we sought to identify the source of this modulation of chemotactic diversity. Previous studies have shown that stochastic gene expression can lead to significant variability in protein levels among isogenic cells, with one study suggesting that proteins in *E. coli* have a baseline variation of 30% in their expression level [43]. Of the dozen or so protein species in the chemotaxis network of *E. coli*, we focused our attention on two, the aspartate receptor Tar and the serine receptor Tsr, since prior studies have demonstrated that the relative ratio of these receptors significantly impact chemotactic behavior, influencing factors such as preference for methyl-aspartate or serine [44, 45], the switch between cryophilic and thermophilic preference [46, 47], and the switch between base-seeking and acid-seeking behavior [48].

To quantify cell-to-cell variability in the Tar/Tsr ratio, we engineered functional fluorescent fusions of the *tar* and *tsr* genes at their native chromosomal loci, fusing *tar* to mCherry and *tsr* to a monomeric form of YFP (Figure 2a) and quantified their single-cell expression levels by fluorescence microscopy (see methods). Using the same parent strain of *E. coli*, MG1655, and identical growth conditions as in our FRET experiments, we measured Tar/Tsr ratio variation under the same conditions in which we assessed chemotactic diversity. When grown in nutrient-rich media to mid-exponential phase (OD = 0.45), cells exhibited substantial cell-to-cell variation in the Tar/Tsr ratio (Figure 2b), with a CV of 0.35. This value is comparable to, though slightly lower than, the Tar/Tsr ratio CV reported by a study that used flow cytometry measurements in a different *E. coli* strain, RP437, which exhibited a CV of 0.45 at OD = 0.51 [46]. The Tar/Tsr ratio CV predicted for the same RP437 strain using single-cell FRET data was 0.5 at OD = 0.45 [27]. These differences are likely attributable to expression differences across *E. coli* strains, which are known to be often substantial even among close relatives [33].

Next, we assessed how the Tar/Tsr ratio evolves as a function of cell density. Using a plate reader, we continuously monitored Tar and Tsr expression and the OD of the cell culture. Cells initially exhibited a low Tar/Tsr ratio, which increased as cell density rose, consistent with previous findings (Figure 2c) [44, 46, 47]. Notably, single-cell fluorescence microscopy revealed that the CV of the Tar/Tsr ratio decreased with increasing cell density, ranging from a CV of 0.43 at OD = 0.30 to a CV of 0.23 at OD = 0.80 (Figure 2d), consistent with modeling predictions of a previous study [27]. This trend mirrors that of the aspartate $K_{1/2}$, whose CV decreases with increasing cell density, and contrasts with the trends observed for serine $K_{1/2}$, whose CV increases with cell density. The increase in the Tar/Tsr ratio at higher optical densities was primarily driven by increased Tar expression, while Tsr levels remained mostly constant (Figure EDF 4). We also observed a strong correlation between Tar and Tsr expression at all optical densities (Figure 2b, inset and EDF 5), which is expected since the genes encoding these receptors—though located in separate operons—are regulated by a common transcriptional regulator, FliA, along with all other chemotaxis genes [46, 49]. Their expression is also likely influenced by global cellular factors that affect the expression of the whole proteome, such as ribosome and polymerase availability [50, 51].

To further investigate how the receptor ratio evolves in different environments, we repeated our plate reader assay in minimal media. In minimal media, the Tar/Tsr ratio remained mostly constant as the cell density increased (Figure 2c) and the distribution of Tar/Tsr ratios was identical across all sampled

optical densities (Figure 2d). This observation aligns with the invariant $K_{1/2}$ distributions observed as a function of OD in minimal media (Figures 1d and 1f). The average Tar/Tsr ratio in minimal media was skewed towards higher Tar levels (Tar/Tsr $\sim$ 3.3; figure 2d), similar to the Tar/Tsr ratio measured at high optical densities in rich media (Tar/Tsr = 3.25 at OD $\sim$ 1.6; figure 2c). Additionally, the CV of the Tar/Tsr ratio was lower in minimal media compared to rich media, with a CV of approximately 0.31, across all optical densities. For both rich and minimal media, the standard deviation in Tar and Tsr protein copy numbers increased with increasing mean copy numbers (EDF 5c), a result consistent with a previous study that characterized the expression of 1018 proteins in *E. coli* using YFP fusions [43].

Our findings suggest that the shift toward a higher Tar fraction at elevated optical densities in rich media (Figure 2c) is the primary driver of increased aspartate sensitivity under these conditions (Figure 1g). Although the total Tsr expression remained approximately constant (EDF 4b), the sharp decrease in serine sensitivity (more than 300%) at higher cell densities (Figure 1g) is likely a consequence of chemoreceptor cluster organization. Tar and Tsr are known to form mixed clusters within the cell membrane [52]; thus, as Tar expression rises with cell density, newly synthesized Tar receptors dilute pre-existing clusters composed primarily of Tsr molecules. This dilution effect reduces overall serine sensitivity despite the approximately constant Tsr expression levels.

2.4 Diversity in the Tar/Tsr ratio is sufficient to quantitatively predict chemosensory diversity

To quantitatively compare the measured diversity of $K_{1/2}$ to the measured diversity in the Tar/Tsr ratio, we turned to theoretical modeling. We employed a mixed-species Monod-Wyman-Changeux (MWC) model [35], which has been successful in fitting a number of *in vivo E. coli* chemotaxis single-cell FRET data [8, 27, 31, 36]. Using this model, we generated a serine dose-response curve for each cell, by fixing the total number of MWC receptors (N_{total}) and using as a single model input their measured Tar/Tsr ratio (see methods). Then, we extracted the single-cell $K_{1/2}$ from each dose-response curve using the same hill function we used to fit experimental FRET data. When comparing the CV of $K_{1/2}$ obtained from our FRET data to the CV of $K_{1/2}$ predicted through the MWC model from our receptor ratio data, we found excellent quantitative agreement across all experimental conditions (Figure 3a). This result alone indicates that a significant portion, if not all, of the observed sensory diversity in the chemotaxis system of *E. coli* can be attributed to the stochastic gene expression of its major chemoreceptors, Tar and Tsr.

To further establish direct causality between receptor expression diversity and $K_{1/2}$ diversity, we generated a population of cells with artificially high levels of receptor ratio variability. To achieve that, we cloned the same Tar-mCherry fusion we engineered on the chromosome of *E. coli* into an inducible vector under the control of a leaky Lac promoter. By transforming the receptor-labeled strain with this vector and tuning its induction level in conjunction with tuning the harvesting OD of the strain (which affects receptor ratio variability in rich media; Figure 2d), we were able to generate a population of cells with approximately the same mean Tar/Tsr ratio as wild-type cells harvested at OD = 0.80 in rich media, but with an approximately two-fold greater Tar/Tsr ratio CV (Figure 3b). We then transformed a strain amenable to FRET experiments with a vector carrying the wild-type Tar receptor under the control of the same leaky Lac promoter. This generated a population of cells with approximately the same mean $K_{1/2}$ as wild-type cells harvested at OD = 0.80 in rich media, but with an approximately three-fold higher $K_{1/2}$ CV (Figure 3c). Importantly, MWC modeling again revealed excellent quantitative agreement between measured $K_{1/2}$ CV and $K_{1/2}$ CV predicted by the model calibrated by receptor-ratio measurements (Figure 3c, inset), thus demonstrating direct causality between receptor expression diversity and diversity in ligand sensitivity.

2.5 Growth environment, not growth time, dictates the Tar/Tsr ratio distribution

We then sought to understand the cause of the observed shift in the Tar/Tsr ratio as a function of cell density in rich media. To test whether the total growth time determines the receptor ratio, we diluted a saturated bacterial culture into fresh rich media at three different final concentrations (Figure 4a). We then harvested all cultures at the same optical density (OD = 0.45). As expected, increasing the dilution

factor by two-fold extended the total growth time by one division cycle (Figure 4b, inset). However, the resulting receptor ratio distributions were identical across all conditions (Figure 4b), demonstrating that growth time has no effect on receptor expression. This result is consistent with a previous study that determined the mean receptor ratio at different growth times using quantitative immunoblotting [44].

To explore whether the chemical environment determines the Tar/Tsr ratio instead, we employed a custom microfluidic chemostat amenable to single-cell microscopy (a "mother machine" [37], see methods). Within the microfluidic chemostat, the growth medium is constantly replenished, and excess cells are washed away, maintaining a constant environment and steady-state growth conditions. We grew cells in rich media to the two extremes of the cell densities examined earlier (OD = 0.30 and OD = 0.80) and measured their receptor ratios. In parallel, we collected the supernatant from both cultures. We then exposed cells growing inside the microfluidic chemostat to the collected supernatant and, after a few hours of growth in each supernatant, we determined their receptor ratios (Figure 4c). Strikingly, we found excellent quantitative agreement between the receptor ratio distributions of the harvested cells and those of cells growing at steady state in the corresponding supernatant (Figure 4d). We also found that growth rate decreases at higher ODs (Figure 4d, inset).

Taken together, these results demonstrate that the receptor ratio of *E. coli* does not follow a predetermined developmental trajectory, nor does it employ a timer-based mechanism that resets upon entry into a new environment. Instead, cells sense changes in their environment and dynamically adjust their receptor ratio—and, by extension, their chemotactic behavior—accordingly.

2.6 Growth rate governs sensory bet-hedging through chemoreceptor ratio modulation

Next, we investigated the molecular mechanism underlying the environment-dependent regulation of the Tar/Tsr ratio. As we showed earlier, the growth rate of cells at early ODs is substantially faster than cells at high ODs (Figure 4d, inset). Therefore, we wondered whether the Tar/Tsr ratio regulation is mediated by growth rate. Indeed, in rich media, growth rate decreases as a function of cell density, slowing as the culture approaches saturation (Figure 5a, inset). In minimal media, however, growth rate remains approximately constant during exponential phase but can be modulated by supplementing the medium with different carbon sources. To examine how growth rate influences the receptor protein concentrations, we measured the Tar protein concentration at different growth rates in rich and minimal media using a plate reader assay (see methods). We found approximately a 10-fold decrease in Tar concentration as the growth rate increased across all environments (Figure 5a, top), consistent with previous studies [53]. Interestingly, Tsr concentration remained constant regardless of growth rate (Figure 5a, bottom). The Tar and Tsr chemoreceptor concentrations obtained from batch, plate reader, data closely matched those obtained via single-cell fluorescence microscopy (Figure 5a).

Taken together, these results suggest that growth rate is the primary — if not sole — determinant of the chemoreceptor ratio. Differences in nutrient availability across growth conditions (e.g., varying cell densities in rich media or different carbon sources in minimal media) modulate growth rate, which in turn regulates chemoreceptor concentrations and thus the Tar/tsr receptor ratio (Figure 5b). This regulation ultimately translates non-linearly into ligand sensitivities (Figure 5c and EDF 8). The non-linear mapping between receptor ratio and $K_{1/2}$ when switching from rich to minimal media likely arises from differences in receptor cluster organization rather than cluster protein stoichiometry. Cryo-electron tomography data have shown that cells grown in minimal media form more tightly-packed receptor clusters compared to cells grown in rich media, despite the similar overall cluster sizes [54]. However, the receptor-to-CheA and receptor-to-CheW stoichiometry is conserved across these two conditions [33, 54], likely because the mocha operon (which includes *cheW* and *cheA*) and meche operon (which includes *tar*), as well as the *tsr* operon are all regulated by FliA [25].

We also found that the degree of sensory diversity, characterized by the CV of $K_{1/2}$, varies as a function of growth rate (Figure 5d). Interestingly, the trends for aspartate and serine are opposite in cells grown in rich media: at fast growth rates, cells exhibit reduced diversity in their sensitivty to serine and increased diversity in their sensitivity to aspartate. This pattern reverses at slow growth rates, where diversity is higher for serine and lower for aspartate. In contrast, in minimal media, diversity remains consistently high for both serine and aspartate, regardless of growth rate. Previous studies have shown

that when grown in rich media, *E. coli* consumes serine at low cell densities (fast growth) and switches to aspartate at higher cell densities (slow growth) [39–41]. Our findings align well with a bet-hedging strategy in which bacterial populations increase diversity in sensing nutrients not yet encountered to boost exploration. Simultaneously, they suppress diversity in sensing current resources for focused exploitation. In line with this strategy, $K_{1/2}$ reaches its lowest value (corresponding to the highest sensitivity) when cells are actively consuming the corresponding ligand (Figure 1g). This anticipatory mechanism primes cells to detect alternative nutrient sources once the current one is depleted. Finally, in environments of greater uncertainty—such as minimal media, where neither serine nor aspartate is present—cells maintain uniformly high chemotactic diversity, ensuring readiness to detect both amino acids when they become available.

Finally, we wondered whether there is a similar bet-hedging mechanism at the level of motile behavior. We quantified the two key parameters that define the random walk of bacteria in absence of chemical gradients: tumble bias and run speed. These parameters have been shown to vary greatly within isogenic populations of *E. coli* cells [28]. We tracked the swimming behavior of motile, wild-type cells—the parent strain used for our FRET-based sensory diversity measurements—using a microfluidic device that allows tracking hundreds of cells simultaneously in a quasi-two-dimensional isotropic environment using phase-contrast microscopy [34]. As expected, we observed substantial diversity in run speed (CV ~ 0.25) and even greater variability in tumble bias (CV ~ 1). However, neither the diversity in run speed nor in tumble bias changed as a function of growth rate (Figure 5e). Similarly, the mean values of both run speed and tumble bias showed only weak dependence on growth rate (EDF 9). The latter observation is consistent with our recent findings in a different *E. coli* strain, RP437, where we reported a constant mean tumble bias across a range of optical densities[34], and it also agrees with an earlier study that reported that the swimming speed of strain HE206 varies only marginally with growth rate [55]. However, it contrasts with older reports describing a non-monotonic relationship between mean run speed and optical density [56]. This discrepancy likely arises from differences in the strains used: RP437 in this earlier study, versus MG1655 here and HE206 in [55].

2.7 Chemosensory diversity boosts collective navigation in contrasting environments via phenotypic filtering

Does the increased sensory diversity we observe under some environments in Figure 5d actually confer a behavioral advantage? Or is the mean sensory phenotype the only important parameter for performance?

To address this question, we devised a bacterial wave speed competition experiment of two populations with the same mean receptor ratio but different receptor ratio variances. To this end, we utilized motile versions of the wild-type and high-variability populations described in Figure 3, each expressing cytosolic YFP to facilitate wave tracking. To decouple sensing from growth, we suspended the cells in a medium that arrests growth, effectively keeping their receptor ratio constant throughout the experiment (see methods). We introduced the two populations in separate microfluidic swim channels [57] containing either 100 μm L-aspartate or 100 μm L-serine (Figure 6a). The cells rapidly formed chemotactic waves by creating a gradient of ligand through consumption and directed movement (Figure 6b) [21, 57, 58]. Both populations migrated faster in serine than aspartate, as it has been shown before [22, 34, 59]. Comparison of the wave velocities of wild-type and high-variability populations revealed a substantial advantage of the high-variability population in both aspartate and serine gradients (Figures 6c and EDF 6). This advantage was not due to differences in individual motility traits, as both populations exhibited identical tumble bias and run speed distributions (EDF 6). These findings demonstrate a clear evolutionary advantage of increased sensory diversity, potentially enabling more diverse populations to colonize new territories faster, thus improving their overall chance of survival in different environments.

To explore the exact mechanism by which high-variability populations climb a ligand gradient faster, we employed the classical chemotaxis assay on soft agar swim plates [60] using motile cells with labeled Tar and Tsr receptors (Figure 6d). On a soft agar swim plate containing nutrient-rich media, *E. coli* cells form a colony with multiple bands of high cell density, the first of which consumes serine [60]. We collected cells from the serine-consuming band and measured their receptor ratios using fluorescence microscopy. At the same time, we measured the receptor ratios of cells in the center of the colony, near the inoculation point. We observed a striking difference between these two populations: cells from

the serine-consuming band had a receptor ratio biased towards higher Tsr and lower Tar, compared to those from the center of the colony (Figure 6e), demonstrating the existence of a receptor ratio sorting mechanism. This finding aligns with our previous theoretical prediction of such sorting mechanism [38] and its experimental demonstration on Tsr selection on swim plates containing a single amino acid [34].

This sorting mechanism is non-genetic, as demonstrated in an experiment using a non-motile strain with labeled Tar and Tsr receptors acting as a biosensor for gene expression. We spread the biosensor strain uniformly across the agar matrix and used its unlabeled wild-type parent strain to establish chemoattractant gradients on the plate. By measuring the receptor ratio of the non-motile strain, we confirmed that there are no changes in the expression of the Tar and Tsr receptors at the center and edge of the colony (Figure 6f), consistent with our previous findings for Tsr expression [34].

During collective migration, this non-genetic sorting mechanism likely enriches the migrating band with cells best suited for climbing attractant gradients: cells with a low Tar/Tsr ratio are selected for in serine gradients, while cells with a high Tar/Tsr ratio are selected for in aspartate gradients. The high-variability population contains cells with both higher and lower Tar/Tsr ratios than the wild-type population. As a result, the sorting mechanism can adapt the phenotypic composition of the migrating band further in the case of the high-variability population, resulting in better chemotactic performance. Since the sorting mechanism is non-genetic, it enables rapid phenotypic filtering even in the absence of growth, as it is the case in our bacterial wave speed competition experiment.

3 Discussion

Phenotypic heterogeneity in isogenic bacterial populations was first noted more than 80 years ago in the context of antibiotic persistence [61, 62]. Within the bacterial chemotaxis system studied here, Spudich and Koshland demonstrated already 50 years ago that isogenic cell populations exhibit substantial behavioral diversity [24]. The advent of single-cell technologies in the last two decades have enabled systematic studies of these phenomena as bet-hedging strategies [6, 27, 31, 63–65], but most have focused on benefits for growth and survival at the single-cell level. In this study, we systematically investigated the mechanisms and consequences of phenotypic diversity in *E. coli* chemotaxis across scales, from stochastic gene expression to population-level collective navigation, under various environmental conditions.

At the intracellular level, we pinpointed the origin of sensory diversity to a single cellular random variable: the ratio between the stochastic expression levels of the two major chemoreceptors Tar and Tsr. We further demonstrated that diversity in the Tar/Tsr ratio, and hence also the sensitivity to chemoeffector ligands, depends on the growth environment. By contrast, we found that diversity in the run-and-tumble motile behavior itself remains constant across environments. The environment-dependent modulation of sensory diversity appears to stem largely from the dependence of *tar* expression on growth rate, whereas *tsr* expression remains nearly constant. Consequently, cells modulate not only the mean ligand sensitivity but also its variance in a manner that is tied to growth rate, without requiring dedicated regulatory pathways that couple sensing of specific nutrients to gene expression. Given that *tar* and *tsr* are located on separate operons, it seems likely that this differential regulation likely occurs at the level of transcription, although our present experiments do not rule out the possibility of post-transcriptional mechanisms.

Operon structure also likely explains the invariance of tumble bias distributions across different growth conditions. Tumble bias is controlled by the expression ratio of two pairs of chemotaxis proteins CheY-CheZ and CheR-CheB [25, 66, 67]. The genes encoding these four proteins are located on the same operon as *tar* (the meche operon), transcribing a single polycistronic mRNA molecule. This organization enforces strong transcriptional [25] and translational [67] coupling between these four proteins and ensures that while the absolute copy numbers of these proteins may vary with growth rate — similar to how Tar copy numbers change (Figure 5a) — their relative ratios remain conserved [25, 67]. On the other hand, the primary determinants of run speed are flagellar number and flagellar length [68]. These parameters appear to remain constant over the growth rate range examined here [55]. This is likely due to the growth-rate independent expression of FliA ($\sigma 28$), the sigma factor responsible for regulating the expression of flagellar filament and motor genes [55]. Thus, while the diversity of sensory response is modulated by the growth environment, we found that key parameters of the motility machinery remained invariant.

Our tests of the consequence of sensory diversity yielded the surprising finding that, beyond single-cell chemotaxis, it can implement bet-hedging at the level of collective migration phenotypes. The hypothesis that *E. coli* exploits sensory diversity to enhance chemotactic navigation [31] has been tested at the single-cell level in agent-based simulations [8], and are consistent with earlier experimental results on single-cell gradient responses in a microfluidic maze [30]. But collective chemotactic migrations require that all cells within the advancing traveling wave of population density to share the same chemotactic drift velocity [21] and hence requires substantial population-level coordination. Naively, a high degree of sensory diversity would seem detrimental to such coordination, given that ligand response sensitivity is a key parameter controlling chemotactic drift velocity [21, 69]. We resolved this apparent paradox by examining gene expression within the migrating collectives. Remarkably, those experiments revealed how cells with a gene expression pattern favorable to fast chemotactic migration (specifically, a low Tar/Tsr ratio within the tested environment with serine as the chemoeffector) are selected by the collective migration behavior itself. The latter phenomenon of phenotype selection within collectively migrating populations was recently predicted [38], and experimentally verified [70] as a mechanism for non-genetic adaptation of population diversity - effectively modulating both the mean and variance of phenotype distributions.

Our results in the present study demonstrate that when combined with environmentally modulated stochastic gene expression, non-genetic diversity adaptation can enable bet-hedging strategies not only at the level of single-cell phenotypes but also for population-level collective behaviors. Moreover, we demonstrated that the environmental modulation of sensory diversity operates through growth rate as a control variable. This enables a collective chemotactic bet hedging strategy that suppresses response diversity toward current growth resources for efficient exploitation, while boosting it toward as yet unencountered resources to enhance exploration. This bet-hedging strategy ensures that in rapidly fluctuating environments, such as terrestrial soils [71] or the mammalian gut [72], a subset of the population is always pre-adapted, priming the entire population to detect and collectively exploit emerging nutrient sources as they become available.

4 Methods

4.1 Strains and plasmids

E. coli strain MG1655 ΔFliC::FLP, a generous gift from Victor Sourjik, was used as a background for all FRET and receptor quantification experiments. For FRET experiments, we conducted an in-frame deletion of the CheRBYZ genes. Subsequently, the gene expressing a glass-adhesive mutant of FliC [27] was cloned at the native FliC locus using homologous recombination, resulting in strain TSS2191. The FRET acceptor-donor pair, consisting of CheY-mRFP1 and CheZ-mYFP (A206K variant), was expressed in tandem from a pTrc99A plasmid under IPTG induction (pSJAB106, [27]). To determine the optimal levels of IPTG induction, we compared the motility of strain TSS2114/pSJAB106 to that of WT strain TSS2096 carrying an empty FRET plasmid (pTrc99A) on soft agar swim plates (EDF 1).

For receptor quantification experiments, *tsr* was translationally fused with mYFP (A206K variant), and *tar* was translationally fused with mCherry, at their respective native chromosomal loci using the same MG1655 ΔFliC::FLP parent strain as in FRET experiments. The cheRB genes were deleted in-frame (yielding strain TSS2155), ensuring comparable Tar receptor expression to that of the strain used for FRET (TSS2191). Since the cheR and cheB genes are located in the same operon as the *tar* gene, factors such as the primary transcript mRNA length can affect the protein copy numbers of Tar.

For FRET experiments involving receptor overexpression, we constructed a high variability strain by transforming TSS2191 with a pTrc99A plasmid expressing wild-type Tar under IPTG induction (pSJAB21). The same FRET acceptor-donor pair used in all other FRET experiments was cloned into a pRZ30 plasmid under NaSal induction (pSJAB196). To quantify receptor overexpression, strain TSS2155 was transformed with a pTrc99A plasmid expressing a Tar-mCherry fusion under IPTG induction (pMV13). Since pSJAB21 and pMV13 are based on the same plasmid backbone, pTrc99A, and are induced at the same level, wild-type Tar and Tar-mCherry are expected to exhibit uniform expression levels.

For swimming competition experiments, wild-type MG1655, a generous gift from Victor Sourjik, was transformed with the same IPTG-inducible pTrc99A plasmid expressing wild-type Tar as in FRET experiments (pSJAB21) to generate a high-variability strain. To maintain uniform growth conditions, the strain used as a wild type for swimming was transformed with an empty pTrc99A plasmid. Both high-variability and WT strains were transformed with a NaSal-inducible pRR31 plasmid expressing cytosolic EYFP to assist with wave tracking (pVS118, gift from Victor Sourjik).

For receptor ratio quantification on swim plates, an adaptation-proficient (CheRB+) version of TSS2155, TSS2144, was utilized, as adaptation is necessary for ascending gradients of attractants. We modulated the motility of TSS2144 by transforming the strain with an arabinose-inducible pBAD33 plasmid expressing WT FliC (pC100B-12, gift from Howard Berg). To determine the optimal levels of arabinose induction, we compared the motility of strain TSS2144/pC100B-12 to that of WT strain TSS2096 carrying an empty pBAD33 plasmid and ΔFliC strain TSS2097 carrying pC100B-12 on rich media soft agar swim plates (EDF 1c). The same strain, TSS2155, without the plasmid expressing WT FliC, was used as a non-motile sensor for gene expression.

Finally, wild-type MG1655 was also used to determine tumble bias and run speed at different growth rates in rich and minimal media.

For an overview of all the strains used in this study, refer to Table 1.

Table 1 Strains used in this study.

Background Strain	Background Strain Source	Background Strain Genotype	Plasmid 1	Plasmid 2
TSS1735	[73]	MG1655 6TetO 6LacO ΔLac	pOB2	-
TSS2096	V. Sourjik	WT MG1655	-	-
TSS2096	V. Sourjik	WT MG1655	pTrc99A	-
TSS2096	V. Sourjik	WT MG1655	pBAD33	-
TSS2096	V. Sourjik	WT MG1655	pSJAB21	pVS118
TSS2096	V. Sourjik	WT MG1655	pTrc99A	pVS118
TSS2097	V. Sourjik	MG1655 ΔFliC	-	-
TSS2097	V. Sourjik	MG1655 ΔFliC	pC100B-12	-
TSS2114	This study	MG1655 ΔCheYZ	pSJAB106	-
TSS2191	This study	MG1655 FliC* ΔCheRBYZ	pSJAB106	-
TSS2191	This study	MG1655 FliC* ΔCheRBYZ	pSJAB21	pSJAB196
TSS2144	This study	MG1655 ΔFliC::FLP Tar-mCherry Tsr-YFP	-	-
TSS2144	This study	MG1655 ΔFliC::FLP Tar-mCherry Tsr-YFP	pC100B-12	-
TSS2155	This study	MG1655 ΔFliC::FLP Tar-mCherry Tsr-YFP ΔcheRB	-	-
TSS2155	This study	MG1655 ΔFliC::FLP Tar-mCherry Tsr-YFP ΔCheRB	pMV13	-

Table 2 Plasmids used in this study.

Plasmid	Source	Product	System	Induction	Resistance
pSJAB21	This study	WT Tar	pTrc99A	30 μM IPTG	amp
pMV13	This study	Tar-mCherry	pTrc99A	30 μM IPTG	amp
pSJAB106	[27]	CheY-mRFP1 CheZ-mYFP	pTrc99A	50 μM IPTG (rich media) 15 μM IPTG (minimal media)	amp
pSJAB196	This study	CheY-mRFP1 CheZ-mYFP	pRZ30	8.5 μM NaSal	cam
pVS118	V. Sourjik	EYFP	pRR31	10 μM NaSal (aspartate waves) 20 μM NaSal (serine waves)	cam
pC100B-12	H. Berg	WT FliC	pBAD33	0.01% Arabinose	cam
pOB2	[73]	LacI-mCherry TetR-EYFP	pBAD24	no induction (relied on promoter leakiness)	amp

Table 3 Parameters used to fit the mixed-species MWC model

Parameter	Value	Reference
C	0.314	[36]
ϵ_0	0.826	[36]
ϵ_A	1.23	[36]
ϵ_s	1.54	[36]
$\tilde{K}$	30 μM	-
$N_{\text{total}} = N_A + N_s$	32 (rich media) 100 (minimal media)	-

4.2 Growth conditions

For experiments conducted in rich media, cells were retrieved from a -80°C glycerol-based stock and inoculated in 2 ml tryptone broth (TB; 1% bactotryptone, 0.5% NaCl, adjusted to pH 7.0) supplemented with 100 μg/mL ampicillin and 34 μg/mL chloramphenicol to maintain plasmids when necessary. The cultures were then incubated overnight at 30°C and 400 RPM until saturation. Subsequently, cells from the saturated overnight culture were diluted 1:50 (except for figure 4b, where the initial dilution was varied) in 10 ml of TB and supplemented with 100 μg/mL ampicillin and 34 μg/mL chloramphenicol, along with appropriate inducer concentrations to induce plasmids (refer to Table 2). For swimming competition experiments in serine gradients cells were grown 1:50 in 20 ml TB, to achieve higher cell counts within the bacterial wave. For supernatant experiments, cells were grown 1:50 in 50 ml TB, to collect a large volume of supernatant. All cultures were grown at 33.5°C with shaking at 250 RPM. Optical density (OD) was measured at 600 nm using a spectrophotometer (Genesys 10vis, Thermo Fisher Scientific), with a permitted error of ±0.01 for all reported OD values.

For experiments conducted in minimal media, cells were retrieved from the same -80°C glycerol-based stock and inoculated in 2 ml H1 minimal salts medium (MMH1; 50 mM KPO4, 0.5 mM MgSO4, 7.6 mM (NH4)2SO4, 1.25 μM Fe2(SO4)3, adjusted to pH 7.0) supplemented with 0.5% v/v glycerol, 0.01% w/v thiamine hydrochloride, and 100 μg/mL ampicillin when necessary to maintain plasmids. Cultures were then incubated for approximately 2 days at 30°C and 400 RPM until saturation. Subsequently, cells from the saturated culture were diluted at least 1:200 in 10 ml of MMH1 supplemented with the same supplements indicated before and appropriate inducer concentrations to induce plasmids (refer to Table 2). Cultures were grown overnight at 33.5 °C with shaking at 250 RPM. As in the experiments conducted in rich media, OD was measured at 600 nm, with a permitted error of ±0.01 for all reported OD values.

For receptor promoter experiments in minimal media, cells were incubated overnight in TB, as described above, and then they were washed with 2 ml MMH1 without glycerol or thiamine hydrochloride three times. Cells were then inoculated in fresh MMH1 supplemented with the indicated carbon source.

4.3 Single-cell FRET microscopy

Single-cell FRET microscopy was performed essentially as described in [74]. Briefly, cells (strain TSS2191/pSJAB106 for WT experiments or TSS2191/pSJAB21/pSJAB196 for high variability experiments) were collected by centrifugation (5 min at 5,000 RPM) and washed twice in 10mL motility media (MotM; 10 mM KPO4, 0.1 mM EDTA, 1 μM L-methionine, and 10 mM lactic acid, adjusted to pH 7.0). Following this, cells were resuspended in MotM and incubated at room temperature (approximately 22°C) for 90 minutes prior to imaging, to allow for further fluorophore maturation. In each experiment, cells immobilized on a glass coverslip were placed in a flow cell under continuous flow of MotM (400 μL/min) regulated by a syringe pump (PHD 2000, Harvard Apparatus). MotM solutions were utilized to incrementally add and remove varying concentrations of the attractants L-serine or L-aspartate (Sigma-Aldrich), with each concentration sustained for approximately 80 seconds.

Imaging was conducted using an inverted microscope (Eclipse Ti-E, Nikon) equipped with an oil-immersion 100x 1.45 NA phase-contrast objective lens (Nikon). Illumination occurred every 2 seconds using a 500 nm LED (pE-4000, CoolLED) with a pulse duration of 20 milliseconds for experiments with serine stimuli or a broad-spectrum LED (SOLA SE, Lumencor) with a pulse duration of 50 milliseconds for experiments with aspartate stimuli. For experiments with serine stimuli, epifluorescent light was split into two channels via a 2-camera image splitter (TwinCam, Cairn Research) equipped with a 580 nm dichroic mirror (Semrock) and two emission filters (520 nm and 593 nm, Semrock), each feeding into identical sCMOS cameras (ORCA-Flash 4.0 V2, Hamamatsu), capturing donor (YFP) and acceptor (RFP) channels separately. For experiments with aspartate stimuli, epifluorescent light was split into two channels via a single camera image splitter (OptoSplit II, Cairn Research) equipped with a 580 nm dichroic mirror (Semrock) and two emission filters (542 nm and 641 nm, Semrock), each projecting side-by-side into a single sCMOS camera (ORCA-Flash 4.0 V2, Hamamatsu), capturing donor (YFP) and acceptor (RFP) channels simultaneously.

FRET images were binned by a factor of 4x4 pixels to maximize their signal-to-noise ratio. All experiments were conducted at room temperature (approximately 22°C). FRET dose-response experiments were highly reproducible (EDF 2). Control experiments verified negligible growth throughout the entire duration of the experiment (EDF 7).

4.4 FRET image analysis

Image analysis was conducted using custom MATLAB scripts. Initially, to compensate for any movement of the flow cell, all images were registered based on the first image of the experiment by employing a rigid transformation. Subsequently, alignment of donor and acceptor channels was achieved through an affine transformation. Following alignment, cell segmentation was performed on the donor (YFP) channel (given its typically higher brightness compared to the acceptor channel), utilizing a modified Otsu algorithm. After segmentation, a rectangular region of interest (ROI) of constant area was defined for each cell. The average YFP and RFP intensities over the ROI were then extracted as a function of time. To mitigate the drift in fluorescence intensities primarily attributed to fluorophore bleaching, the FRET ratio of each cell (defined as RFP/YFP) was fitted with a double exponential function. Subsequently, the FRET ratio was divided by the double exponential and normalized between one (unstimulated steady-state activity) and zero (activity upon addition of a saturating dose of the attractant serine or aspartate), which corresponds to the kinases CheA in the cell being fully active and fully inactive, respectively. Therefore, the kinase activity of each cell is given by:

$$\alpha(t) = \frac{FRET(t) - FRET_{\text{saturating}}}{FRET_{\text{steady-state}} - FRET_{\text{saturating}}}$$

4.5 MWC Model

To obtain a distribution of $K_{1/2}$ parameters from the receptor expression data, we employed the mixed-species MWC model as described in [36]. The expression for the normalized response to L-serine is:

$$a = \frac{\epsilon_0 \epsilon_s^{N_s} \epsilon_A^{N_A} \left(1 + C\frac{[L]}{\tilde{K}}\right)^{N_s}}{\left(1 + \frac{[L]}{\tilde{K}}\right)^{N_s} + \epsilon_0 \epsilon_s^{N_s} \epsilon_A^{N_A} \left(1 + C\frac{[L]}{\tilde{K}}\right)^{N_s}}$$

where ϵ_A, ϵ_s, and ϵ_0 are the L-serine binding energies to Tar, Tsr, and to the three minor receptors, respectively. The number of Tsr receptors is denoted by N_s, while the number of Tar receptors is denoted by N_A. The vector $[L]$ represents the concentrations of L-serine and C and $\tilde{K}$ describe the ligand dissociation constant for the active state of the receptor, as:

$$K_A = \frac{\tilde{K}}{C}$$

All variables apart from parameters N_s and N_A were kept constant for all cells and are given in Table 3. The L-serine concentration vector $[L]$ was defined as a logarithmically spaced vector between 0.1 and 10,000. To transform the measured Tar/Tsr ratio to the MWC receptor count N_s and N_A, we used:

$$N_s = \frac{N_{\text{total}}}{\frac{\text{Tar}}{\text{Tsr}} + 1}$$

$$N_A = N_{\text{total}} - N_s$$

The normalized expression for the response to L-serine yielded a sigmoidal function between 0 and 1 for all measured receptor ratios in rich media. For minimal media experiments, a fraction of cells with extreme receptor ratios did not produce a response between 0 and 1. These data points were excluded from $K_{1/2}$ extraction. It is likely that these cells correspond to the fraction of non-motile cells, which is known to be larger for cells grown in minimal media compared to cells grown in rich media [22]. Finally, to extract $K_{1/2}$ from the MWC normalized response to L-serine we used a Hill function of the form:

$$a = \frac{1}{1 + \left(\frac{[L]}{K_{1/2}}\right)^H}$$

where $K_{1/2}$ and H are the fit parameters. The same Hill function was used to fit experimental dose-response data.

4.6 Colony expansion rate quantification

To calibrate the FRET pair (pSJAB106) and WT FLiC plasmid expression (pC100B-12), we assessed the expansion rate of bacterial colonies carrying the plasmid of interest (strain TSS2114/pSJAB106 or TSS2097/pC100B-12) alongside WT colonies (strain TSS2096) carrying an empty version of the same plasmid (EDF 1). Cells grown in rich media were collected at OD = 0.45 and cells grown in minimal media were collected at OD = 0.30 and diluted to OD = 0.01 using fresh media. Then, 10 μL of cell culture was inoculated in the center of semi-solid agar plates. Liquid media and agar plates were supplemented with appropriate antibiotics and inducers, refer to Table 2. All colony expansion rate experiments were conducted at 33.5°C and 100% humidity. For each experiment, six swim plates were imaged simultaneously using a custom-built motorized turret. Images of each plate were taken every 10 minutes using a Canon DSLR camera. To extract the expansion rate, the diameter of the expanding colony was determined as a function of time by fitting an ellipse with an eccentricity smaller than 0.2 using the MATLAB regionprops function on every image, after subtracting the first image of each plate (taken before the colony had formed).

4.7 Chemoreceptor copy number quantification

The quantification of Tar and Tsr chemoreceptor copy numbers was conducted using both a plate reader assay and single-cell fluorescence microscopy. For growth and chemoreceptor copy number measurements in the plate reader (Victor X3 2030 Multilabel reader, PerkinElmer), cells (strain TSS2155) were diluted from an overnight saturated culture into fresh media (dilution ratios 1:50 for TB and 1:200 for MMH1) and 200μL of cell culture was aliquoted into each well of a 96-well plate (96-well Clear Flat Bottom TC-treated Microplate, Corning). Cultures were grown at 33.5 °C with double orbital shaking with a shaking amplitude of 2 mm until they reached saturation. Fluorescence (YFP and mCherry) and optical density (OD600) were measured every 15 minutes. The autofluorescence of the non-fluorescent parent strain of TSS2155, TSS2097, grown in the same well plate, was subtracted from all fluorescent measurements. The OD units of the plate reader were calibrated against the OD units of the spectrophotometer used to measure the OD of the batch cultures for single-cell fluorescence microscopy experiments (Genesys 10vis, Thermo Fisher Scientific) by constructing a calibration curve through serial dilution of a saturated culture. The receptor ratio units measured with the plate reader were calibrated against mean receptor ratios obtained from fluorescence microscopy for the same optical densities.

For single-cell quantification of chemoreceptor copy numbers, cells (strain TSS2155 for WT experiments or TSS2155/pMV13 for high variability experiments) were harvested from batch TB or MMH1 culture at the appropriate OD by centrifugation (5 min at 5,000 RPM). The cells were then washed twice in 10mL minimal motility media (minimal MotM; 10 mM KPO4 and 0.1mM EDTA, adjusted to pH 7.0). After washing, cells were diluted in minimal motility media, allowed to mature, and plated on agarose pads (1.5% agarose in minimal MotM). The pads were left to dry for 10 minutes before immediate imaging.

Imaging was performed using an inverted microscope (Eclipse Ti-E, Nikon) equipped with an oil-immersion 100x 1.45 NA phase-contrast objective lens (Nikon). YFP and mCherry fluorescence was excited using an LED system (pE-4000, CoolLED), and emissions were captured sequentially using a multi-band filter (Semrock) and directed into two identical sCMOS cameras (ORCA-Flash 4.0 V2, Hamamatsu) via a 2-camera image splitter (TwinCam, Cairn) equipped with a 580 nm dichroic mirror (Semrock). Approximately 20 fields of view, totaling around 1000 cells, were typically imaged per experiment. Measurements took place at room temperature (approximately 22°C). A control experiment revealed that nearly zero growth took place during the total duration of the experiment (EDF 7b).

To ensure accurate determination of the Tar/Tsr ratio, excitation pulse durations and intensities for YFP and mCherry were calibrated using a two-color fluorescent repressor-operator system (FROS) standard [73]. This FROS strain (strain TSS1735/pOB2) contained six mCherry- and YFP-repressor fusions on its chromosome. By using a 100 ms 500 nm LED excitation pulse for mYFP and a 200 ms 580 nm LED excitation pulse for mCherry (both at maximum intensity), nearly identical emission intensities for mCherry and YFP were achieved, effectively equating the measured mCherry/YFP fluorescent intensity ratio to the true Tar/Tsr receptor abundance ratio (EDF 3). To avoid movement of the chromosome due to diffusion during the measurement, cells were chemically fixed by incubating them for 10 min at room temperature in a 4% paraformaldehyde solution (Sigma-Aldrich).

4.8 Chemoreceptor image analysis

In each field of view, a set of images comprising one phase-contrast, one YFP, and one mCherry channel image was obtained. Alignment of images from the two cameras was performed using a custom MATLAB script through an affine transformation. Subsequently, cell segmentation was conducted on the phase-contrast channel utilizing a modified Otsu algorithm. We used the phase-contrast channel to segment the cells instead of one of the two fluorescent channels to ensure that cells with low fluorescence (and hence low receptor expression) are included in the analysis. Following segmentation, background subtraction was applied to each image, and a rectangular ROI of the same area is defined for each cell. The average mCherry and YFP fluorescent intensities over the ROI are extracted for every cell. When indicated, average fluorescent intensities are normalized by cell area, determined by fitting an ellipse on the detected cells in the phase-contrast channel

4.9 Fabrication of microfluidic chemostats

Microfluidic chemostats, commonly referred to as "mother machines," were fabricated using the silicone polymer polydimethylsiloxane (PDMS). The master mold for the PDMS device is a silicon wafer on which features are imprinted on a layer of SU-8, an epoxy-based negative photoresist [75]. Features are imprinted using UV light exposure through two separate photomasks. The first layer of the device comprises an array of shallow and narrow growth channels measuring 25 μm in length and 0.96 μm in height. To allow the tight confinement of cells of different widths and hence accommodate growth at different growth rates, the width of the growth channels varies within the range of 0.7 μm to 1.2 μm, with a step size of 0.1 μm. The edges of the channels were smoothed to reduce optical aberrations during phase-contrast imaging [76]. The second layer of the device features a deeper and wider feeding channel with low fluidic resistance, enabling rapid liquid exchange. The feeding channel measures 12 mm in length, 100 μm in width, and 32.5 μm in height. The designs for the two different layers were created using CAD software (klayout) and transferred onto two separate quartz photomasks (Photronics). Fabrication of the silicon master mold was conducted at AMOLF's cleanroom facilities. Following fabrication, a hydrophobic coat of chlorotrimethylsilane (Sigma-Aldrich) was applied via vapor deposition.

To cast PDMS devices, the master mold was coated with a layer of degassed 10:1 PDMS:curing agent mixture (Sylgard 184, Dow Corning) and cured at 80°C for 1 hour. After cooling the wafer to room temperature, individual devices were cut and separated from the wafer, and inlets and outlets for each feeding channel were created using a 0.75-mm biopsy punch (World Precision Instruments). To remove any residual uncured PDMS, devices were immersed in a pentane bath for 2 hours and then in an acetone bath twice for 2 hours each. The PDMS devices were then allowed to dry at room temperature overnight. To facilitate bonding, the PDMS devices were cleaned with transparent adhesive tape (Magic Tape, Scotch) and treated, along with glass-bottom dishes (GWST-5040, WillCo Wells), in a plasma cleaner (PDC-002, Harrick Plasma). Following a 60-second exposure to ambient air plasma under a 300 mTorr vacuum, the devices were laminated onto the glass-bottom dishes and baked on an 80°C hot plate for 5 minutes to establish a covalent bond. In order to passivate the PDMS surface and prevent cell attachment, the devices were incubated with a 10 mg/ml BSA solution for 45 minutes at 37°C to allow the BSA solution to be drawn into the growth channels via evaporation through the gas-permeable PDMS. The devices were then immediately used for experiments.

4.10 Supernatant experiments

For supernatant experiments, cells (TSS2155) grown in rich media were collected at OD = 0.30 and OD = 0.80 by centrifugation (5 min at 5,000 RPM) and washed twice in 10mL minimal MotM. The supernatant of those cultures was filtered using a 0.22 μm syringe filter and stored at 3°C until the experiment. The washed cells were imaged following the same protocol as for all receptor-labeled cells, with the exception that imaging took place at 33.5°C, so the measured receptor ratios are directly comparable to those of growing cells in the microfluidic chemostat.

Simultaneously, 10μL of the original OD = 0.30 culture was injected into a microfluidic chemostat through its inlet. The inlet and outlet of the chemostat were then sealed with adhesive tape (Magic Tape, Scotch) to prevent flow and the entire device was centrifuged for 20 minutes at 800 RPM, orienting the growth channels parallel to the centrifugal force axis to force cells into the growth channels. Following centrifugation, the device was incubated for 2 hours at 33.5°C, to allow for additional cells to enter the growth channels via diffusion. Subsequently, the collected supernatants were placed inside sterile glass reservoirs pressurized to 130 kPa using nitrogen. These reservoirs were then connected through separate tubes to a distribution valve (M Switch, Fluigent), which in turn was connected to the microfluidic device through a tube plugged into its inlet. The distribution valve input, and hence the growth environment of the cells, was controlled through a custom MATLAB script.

To extract the receptor ratio of the growing cells, the microfluidic device was imaged using the same microscopy setup and imaging settings we employed for all receptor-labeled cell experiments. However, imaging occurred at 33.5°C, instead of room temperature, to facilitate cell growth. To extract the morphology of the cells and to determine a segmentation mask, phase-contrast images were acquired from a single field of view every minute. Furthermore, at 20-minute intervals, corresponding to the maximum

division rate observed in our experiment, one mCherry and one YFP image were acquired to quantify receptor expression.

4.11 Image analysis of microfluidic chemostat experiments

To accurately segment bacteria cells growing in the microfluidic chemostat, we trained a machine learning model to predict the outline of each cell. We used a convolutional neural network (CNN) based on the U-Net architecture [77, 78] to transform the original microscopy images into maps of cell outlines using custom Python scripts. To train the network, we simultaneously acquired fluorescent images, using the bright CheY-mRFP1 fusion, and phase-contrast images of growing cells. Subsequently, we manually created binary masks of all cell outlines in 500 CheY-mRFP1 512x512 pixel images and augmented this dataset using geometric transformations such as scaling, translation, and rotation. This augmented dataset was then utilized to train the CNN.

Following the training phase, we applied the CNN to transform 2000 CheY-mRFP1 frames, distinct from the original training dataset, without any post-processing of the images. The CNN generated unique 512x512 pixel output matrices for each image, with high scores corresponding to cell outlines while cell bodies and the background contained nearly zero scores. We then re-trained the CNN using the phase-contrast images and the binary masks created by the CNN based on CheY-mRFP1 images as inputs. Additionally, we augmented these datasets further using geometric transformations. Through this training method, we increased our training dataset by a factor of 4, while manually segmenting only CheY-mRFP1 images, which are substantially easier to segment compared to phase-contrast images due to the brightness of the fluorescent fusion protein and the near-zero background fluorescence.

The primary advantage of using phase-contrast images for cell segmentation is the elimination of the need for an additional fluorescent protein and imaging channel, as well as the avoidance of phototoxicity associated with fluorescent imaging. Visual inspection of the transformed images revealed consistent cell masks produced by the CNN, irrespective of whether the original image was obtained through fluorescence or phase-contrast microscopy.

Subsequently, the CNN output binary matrices underwent further processing by thresholding using a modified Otsu algorithm and removing small clusters of unconnected pixels, effectively setting only the pixels corresponding to cell outlines to unity and every other pixel to zero. Then, alignment of images from the two cameras was performed using a custom MATLAB script employing an affine transformation. All images were then registered based on the first image of the experiment using a rigid transformation to correct for movement of the microfluidic device. Fiducial markers in the form of growth channel numbering were incorporated into the device to assist with image registration. Finally, individual growth channels were cropped out by summing the fluorescence of both channels and detecting peaks in the fluorescence intensity profile.

For cell segmentation, we employed the MATLAB regionprops function, which detects cells in the CNN-transformed images as elliptical objects. For each cell, we determined its minor and major axes, along with the x- and y-coordinates of its centroid. The centroid was then tracked across all frames, under the assumption that interframe movement could not exceed a threshold defined as one quarter of the shortest cell length in any given image. Movement was considered only along the long axis of the growth channel, as the cells were constrained along their width, thereby minimizing tracking to a one-dimensional problem. Divisions were identified by abrupt changes in cell length (the major axis of the fitted ellipse), coupled with an increase in cell count. Conversely, a reduction in cell count, alongside the disappearance of centroids near the origin of the growth channel, indicated cells exiting towards the feeding channel. Subsequently, the minor and major axes of the fitted ellipses were utilized to define rectangular segmentation masks, facilitating the extraction of fluorescent intensity for each cell across all frames. Areas devoid of cells were used to extract the background intensity of each frame.

4.12 Fabrication of microfluidic devices for swimming competition experiments

For swimming competition experiments, we utilized a microfluidic device comprising a long linear channel with dimensions of 1.2 mm x 2 cm x 100 μm (width, length, height). These devices were fabricated

following the procedure outlined in [57]. To establish a cost-effective method of producing devices without the necessity for silicon wafer masters, we manufactured epoxy molds utilizing the silicon wafer-molded PDMS devices as masters [79]. The devices were submerged in a degassed mixture of epoxy and hardener (epoxacast 690, Smooth-On) in a 10:3 ratio, and the mixture was allowed to solidify at room temperature for 2 days. Similar to silicon wafers, a hydrophobic coat of chlorotrimethylsilane was applied via vapor deposition.

To cast PDMS devices, the master mold was coated with a layer of degassed 10:1 PDMS:curing agent mixture (Sylgard 184, Dow Corning) and cured at room temperature for 2 days due to the low glass transition temperature of the epoxy mold. Individual devices were then cut and separated from the wafer, and a 0.75-mm outlet and a 2-mm cell reservoir were created on either side of the linear channel using biopsy punches (World Precision Instruments). Subsequently, the devices underwent cleaning with transparent adhesive tape (Magic Tape, Scotch), followed by rinsing sequentially with isopropanol, methanol, and Millipore-filtered water. After drying the devices using nitrogen, they were treated, alongside glass-bottom dishes (GWST-5040, WillCo Wells), in a plasma cleaner (PDC-002, Harrick Plasma). Following a 60-second exposure to ambient air plasma under a 300 mTorr vacuum, the devices were laminated onto the glass-bottom dishes and baked on an 80°C hot plate for 5 minutes to establish a covalent bond. Then, after cooling the devices to room temperature, they were immediately utilized for experiments.

4.13 Swimming competition experiments

For swimming competition experiments, cells (TSS2096/pTrc99A/pVS118 for WT experiments or TSS2096/ pSJAB21/pVS118 for high-variability experiments) grown in rich media were collected at the appropriate OD by centrifugation (5 min at 5,000 RPM) and washed twice in 10mL MotM. Cells were then concentrated to OD = 1.0 for aspartate wave experiments or OD = 2.0 for serine wave experiments. In parallel, the microfluidic linear channel devices were filled with either 100μM L-aspartate or 100μM L-serine (Sigma-Aldrich) in MotM supplemented with 0.05% w/v polyvinylpyrrolidone-40 (Sigma-Aldrich) from the 0.75-mm outlet. Subsequently, excess liquid was removed from the 2-mm cell reservoir and 5μL cell suspension was loaded gently into the reservoir. The outlet was sealed with adhesive tape (Magic Tape, Scotch) to prevent flow due to differences in hydrostatic pressure across the device.

Migrating waves in swimming competition experiments were imaged immediately after cell loading using an inverted microscope (Eclipse Ti-E, Nikon) equipped with an environmental chamber (Okolab) set to a temperature of 33.5°C and 80% humidity. YFP images of the bacterial wave were captured through a 10x 0.30 NA objective lens (Nikon). The field of view was illuminated with a 500 nm LED (pE-4000, CoolLED) set to maximum intensity, with an exposure time of 100 ms. Images were recorded by a sCMOS camera (ORCA-Flash 4.0 V2, Hamamatsu). To track the bacterial wave, the microscope stage (MicroStage, Mad City Labs) was programmed using a custom MATLAB script to translocate every 10 seconds by one frame width (1.33 mm). Six consecutive images were taken for each sweep, and full sweeps occurred every 60 seconds until the wave had traversed all six consecutive fields of view. A control experiment revealed that nearly zero growth took place during the total duration of the experiment (EDF 7c and EDF 7d).

For wave speed analysis, raw YFP images were stitched into single images for each sweep using custom MATLAB scripts. The initial stitched image, which lacked cells, was subtracted from subsequent images to eliminate imaging artifacts. Images were then segmented using a modified Otsu algorithm, filtering out objects smaller than 100 pixels. Subsequently, image intensities were normalized between one and zero, and a Gaussian function was fitted to the intensity profile along the long axis of the channel (EDF 6). The wave position was determined by identifying the peak of each Gaussian, and velocity was calculated by extracting the distance between successive peaks and dividing it by the time between sweeps (60 seconds).

4.14 Chemoreceptor copy number quantification on swim plates

Experiments with swim plates were performed similarly to what we reported on [34].

Briefly, to quantify the chemoreceptor copy number of cells forming colonies on swim plates, cells (strain TSS2144/pC100B-12) grown in rich media were collected at OD = 0.45 and diluted to OD = 0.01 using fresh media. Then, 10 μL of cell culture was inoculated in the center of semi-solid agar plates. The agar plates were made using rich media, as described above, supplemented with 0.26% bacteriological agar

(Avantor). Liquid media and agar plates were supplemented with appropriate antibiotics and inducers, refer to Table 2. The plates were incubated at a temperature of 33.5°C and 100% humidity until the colonies reached the edge of the plate. Cells from the center and the edge of the migrating colony were collected using pipette tips and diluted into minimal MotM for subsequent fluorescent imaging. To quantify chemoreceptor numbers, we followed the same fluorescent imaging protocol as for receptor-labeled cells grown in liquid cultures.

For experiments involving non-motile cells used as biosensors for gene expression, cells (strain TSS2144) grown in rich media were collected at OD = 0.45 and mixed with fresh rich media supplemented with 0.26% bacteriological agar to achieve a final OD = 0.01. Swim plates were allowed to solidify at room temperature for 2-3 hours, following which 10 μL of OD = 0.01 motile cell culture (strain TSS2096) was inoculated in the center of the semi-solid agar plates. The motile population of cells shapes the gradient of the plate, ensuring that the non-motile biosensor strain encounters the same local environment as motile cells. Once the migrating cell colony reached the edge of the plate, cells from the center and the edge of the colony were collected using pipette tips and diluted into minimal MotM for subsequent fluorescent imaging.

4.15 Fabrication of microfluidic devices for single cell swim tracking

To track the run-and-tumble motion of single cells, we utilized a microfluidic device comprising a long linear channel with dimensions of 0.5 mm x 3 cm x 60 μm (width, length, height). These devices were fabricated following the procedure outlined in [34]. Briefly, the master mold was coated with a layer of degassed 10:1 PDMS:curing agent mixture (Sylgard 184, Dow Corning) and cured at 80°C for 12 hours. After cooling the wafer to room temperature, individual devices were cut and separated from the wafer, and a 0.75-mm outlet and a 0.75-mm inlet were created on either side of the linear channel using biopsy punches (World Precision Instruments). Subsequently, the devices underwent cleaning with transparent adhesive tape (Magic Tape, Scotch), followed by rinsing sequentially with isopropanol, methanol, and Millipore-filtered water. A 22 mm x 50 mm glass coverslip was rinsed sequentially with acetone, isopropanol, methanol, and Millipore-filtered water. After drying the devices and the coverslips using nitrogen, they were treated in a plasma cleaner (PDC-32G, Harrick Plasma). Following a 60-second exposure to ambient air plasma under a 300 mTorr vacuum, the devices were laminated onto the glass coverslips and baked on an 80°C hot plate for 5 minutes to establish a covalent bond. Then, after cooling the devices to room temperature, they were immediately utilized for experiments.

4.16 Swim tracking experiments

For swim tracking experiments, WT cells (strain TSS2096) grown in rich or minimal media were collected at the appropriate OD by centrifugation (5 min at 5,000 RPM) and washed twice in 10mL MotM supplemented with 0.05% w/v polyvinylpyrrolidone-40 (Sigma-Aldrich). Cells were then diluted to an OD of 0.001. Subsequently, 10 μL of the mixture was introduced into the device from the inlet and excess liquid was removed from the outlet. Both the outlet and the inlet were then sealed with adhesive tape (Magic Tape, Scotch) to prevent flow due to differences in hydrostatic pressure across the device.

Swimming cells were imaged immediately after cell loading using an inverted microscope (Eclipse Ti-E, Nikon) equipped with a custom environmental chamber set to a temperature of 30°C and 50% humidity for experiments in Figures 5e and EDF 9 or 33.5°C and 80% humidity for experiments in EDF 6c and EDF 6d, to match the environmental conditions of swimming competition experiments. Phase-contrast images of swimming bacteria were captured through a 4x 0.13 NA phase objective lens (Nikon). Images were recorded by a sCMOS camera (ORCA-Flash 4.0 V2, Hamamatsu) at 20 frames per second.

To detect and track cells and extract their tumble bias and run speed, a custom MATLAB script was used as described in [80]. Trajectories shorter than 10 seconds were excluded for further analysis. In a typical experiment, 4 fields of view where imaged for 200 seconds each, containing a total of at least 1000 cell trajectories.

4.17 Growth rate measurements

To assess the growth rate of the FRET (TSS2191/pSJAB106), receptor-labeled (TSS2155), and WT (TSS2097) strains, we employed a microplate reader (Epoch 2 microplate reader, BioTek). Overnight cultures in rich media were diluted 1:50 into fresh media and overnight cultures in minimal media were diluted 1:200 into fresh media. For the FRET strain, the appropriate antibiotic and inducer concentrations were added to the media (refer to Table 2). Subsequently, 200 μL of diluted cells were aliquoted into each well of a 96-well plate (Costar 3595, Corning) and loaded into the plate reader. The plates were incubated at 33°C while continuously shaking in a double orbital pattern (1 mm radius, 807 cpm). The OD of each well was measured every 10 minutes for 12 hours for rich media and every 20 minutes for 24 hours for minimal media. The growth rates measured in the plate reader were within 10% of those obtained by sampling the shaking batch culture used for microscopy experiments.

4.18 Growth rate and cell volume quantification

The quantification of *tar* and *tsr* promoter activities as a function of growth rate was conducted using a plate reader assay, as described above. The growth rate of the bacteria is expressed as doublings per hour and is calculated as:

$$\text{growth rate} = \frac{\log_{10}(\text{OD}_{t_2}) - \log_{10}(\text{OD}_{t_1})}{(t_2 - t_1)\log_{10}(2)}$$

5 Acknowledgments

We thank Simone Boskamp for her invaluable assistance with cloning and transformations and Dimitry Lamers for assisting with the microfluidic chemostat wafer fabrication. We also thank Lam Vo for providing the microfluidic device for wave tracking, Jyot Antani for helping set up the cell tracking experiment, and Gustavo Madeira Santana for helping set up the FRET experiment. We thank Marko Kamp for microscopy support and Brahim Ait Said for software support. We thank Victor Sourjik and Howard Berg for providing plasmids and strains that were used in this study. Finally, we thank John S. Parkinson, Jeremy Moore, Keita Kamino, Lam Vo, Diana Valverde Mendez, and Evan Usher for helpful discussions.

6 Author contributions

FA, TSS, and TE conceived the study. FA performed experiments. RJ assisted with receptor quantification experiments. FA analyzed the data and wrote the manuscript. FA, RJ, TSS, and TE edited the manuscript. This work was supported by NIGMS awards R01GM106189 (TE and TSS), R01GM138533 (TE), and R35GM158058 (TE).

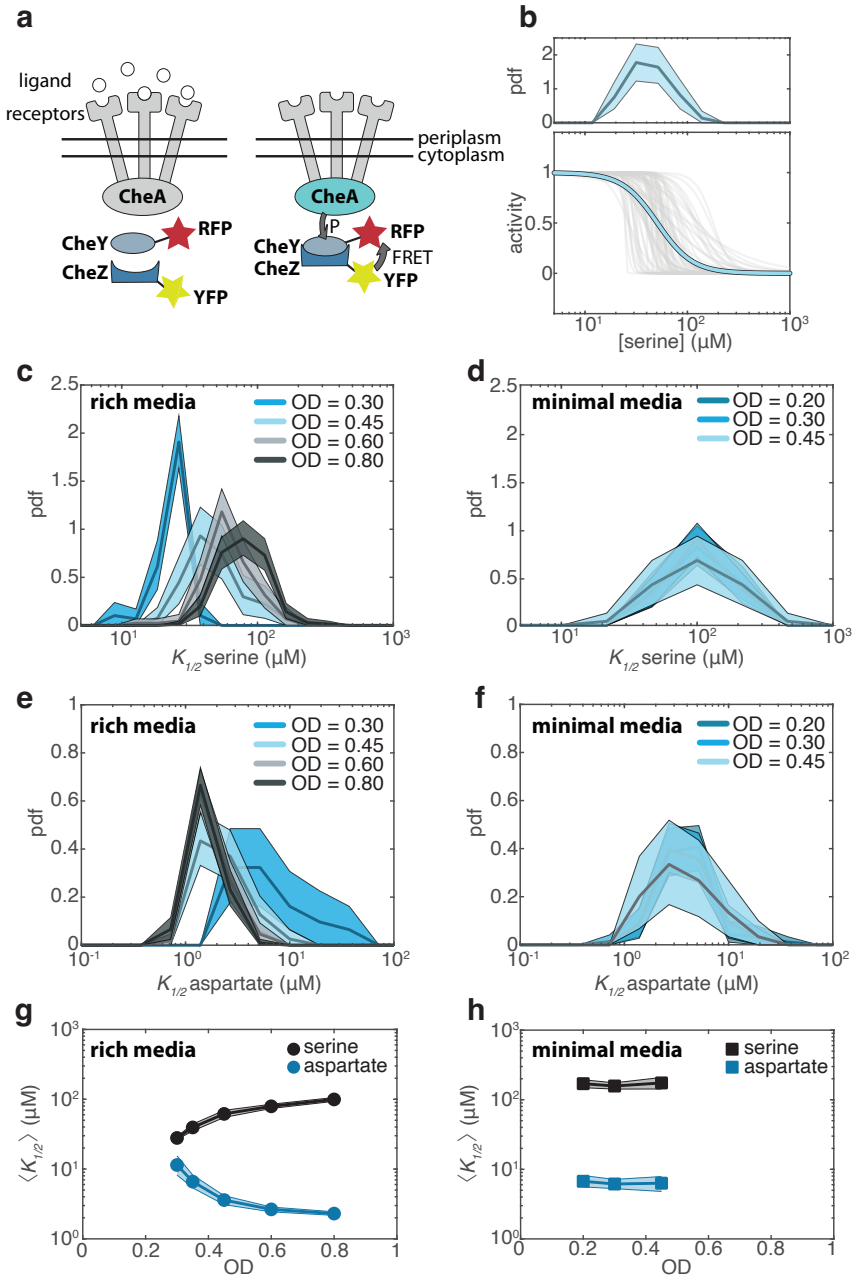

Fig. 1 Single-cell FRET reveals extensive environment-dependent diversity in ligand sensitivity across an isogenic bacterial population. **(a)** Schematic of the *in vivo* FRET assay. The kinase CheA phosphorylates the response regulator CheY producing CheY-P in the absence of ligand binding to receptors. CheZ dephosphorylates CheY. The FRET signal between fluorescently labeled CheZ and CheY is proportional to the CheA activity. **(b)** (Bottom) single-cell (gray) and population-averaged (blue) Hill function fits to L-serine dose-response data obtained from a single experiment using adaptation-deficient cells grown to OD = 0.45 in rich media. (Top) Histogram of the inverse of ligand sensitivity values, $K_{1/2}$, extracted from the single-cell dose response curves shown above. **(c)** Histograms of L-serine $K_{1/2}$ values obtained from single-cell dose-response curves for cells grown to different ODs in rich media. Each distribution represents data from a single experiment. Shaded areas indicate 95% confidence intervals obtained via bootstrap resampling of the data. **(d)**Same as (c), but for cells grown in minimal media **(e)** Histograms of L-aspartate $K_{1/2}$ values obtained from single-cell dose-response curves for cells grown to different ODs in rich media. Each distribution represents data from a single experiment. Shaded areas indicate 95% confidence intervals obtained via bootstrap resampling. Figure legend and color scheme are consistent with panel (c). **(f)** As in (e), but for cells grown in minimal media. Figure legend and color scheme are consistent with panel (d). **(g)** Scaling of mean L-serine and L-aspartate $K_{1/2}$ as a function of OD for cells grown in rich media. Shaded areas indicate 95% confidence intervals obtained via bootstrap resampling. **(h)** Same as (g), but for cells grown in minimal media.

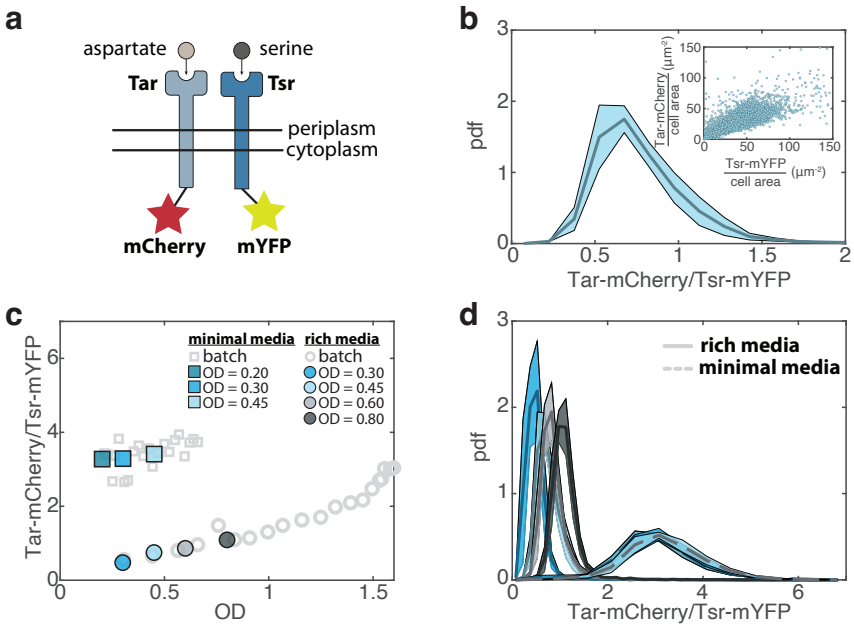

Fig. 2 Fluorescent fusions of major chemoreceptors reveal extensive environment-dependent diversity in chemoreceptor composition across an isogenic bacterial population. **(a)** Schematic of the receptor protein quantification assay. The chemoreceptor Tar, which binds the amino acid L-aspartate, is fused at its native chromosomal locus to the fluorophore mCherry. The chemoreceptor Tsr, which binds the amino acid L-serine, is fused at its native chromosomal locus to the fluorophore mYFP. Imaging parameters were calibrated using a two-color fluorescent repressor-operator system (FROS) standard to equate the measured mCherry/YFP fluorescent intensity ratio to the true Tar/Tsr receptor abundance ratio (EDF 3). **(b)** Histogram of the Tar/Tsr chemoreceptor ratio measured with fluorescence microscopy for cells grown to OD = 0.45 in rich media, growth condition identical to the one used in figure 1b. The solid line represents the mean of four independent biological replicates, while shaded areas indicate the standard error of the mean across replicates. Inset: Correlation between Tar-mCherry and Tsr-mYFP expression levels. Each point represents a single cell, derived from four independent biological replicates. Tar and Tsr expression levels are strongly correlated ($R^2 = 0.70$). **(c)** Relationship between the Tar/Tsr chemoreceptor ratio and OD for cells grown in rich (circles) and minimal (squares) media. Gray hollow points represent the mean of 40 technical replicates measured using a plate reader. Colored points represent the mean Tar/Tsr ratio measured via fluorescence microscopy from four (rich media) or three (minimal media) independent biological replicates for each OD. **(d)** Histograms of the Tar/Tsr chemoreceptor ratio measured via fluorescence microscopy for cells grown to different ODs in rich (solid line) or minimal (dashed line) media. Lines represent the mean distribution of all independent biological replicates, while shaded areas indicate the standard error of the mean across replicates. The color scheme is consistent with panel c.

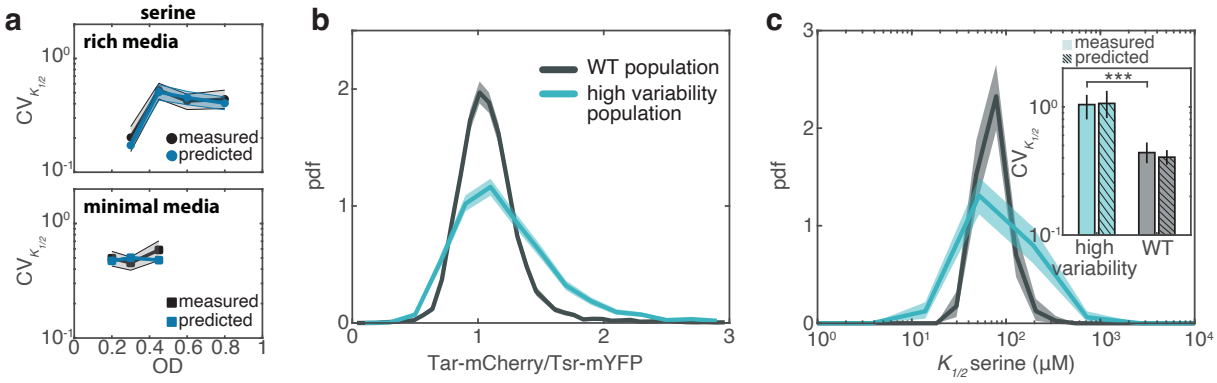

Fig. 3 Prediction of chemosensory diversity from Tar/Tsr ratio variation, and establishing causality. **(a)** (Top) Black points represent the measured coefficient of variation (CV) of the inverse of ligand sensitivity, $K_{1/2}$, as a function of OD in rich media, obtained from the single-cell dose-response experiments in Figure 1c. Blue points represent the predicted CV of $K_{1/2}$ as a function of OD in rich media, derived through the mixed-species MWC model using single-cell receptor ratio data from Figure 2d as an input. Shaded areas indicate 95% confidence intervals obtained through bootstrap resampling. (Bottom) Same as the top panel, but for cells grown in minimal media. The CV was either measured from the single-cell dose-response experiments in Figure 1d (black points) or predicted from the mixed-species MWC model using single-cell receptor ratio data from Figure 2d as input (blue points). The total number of MWC receptors (N_{total}) was fixed to 32 for all rich media experiments and 100 for all minimal media experiments. **(b)** Histograms of the Tar/Tsr chemoreceptor ratio measured via fluorescence microscopy for wild-type cells (WT population; replotted OD = 0.80 data from Figure 2d) and for a population with artificially increased Tar/Tsr ratio variability (high variability population). Solid lines represent the histograms of all Tar/Tsr ratios from four independent biological replicates (WT population) or a single experiment (high variability population). Shaded areas indicate 95% confidence intervals obtained through bootstrap resampling. **(c)** Histograms of L-serine $K_{1/2}$ values obtained from single-cell dose-response curves for wild-type cells (WT population; replotted OD = 0.80 data from figure 1c) or cells with artificially increased Tar/Tsr ratio variability (high variability population). Solid lines represent the histograms from a single experiment, with shaded areas indicating 95% confidence intervals obtained through bootstrap resampling. Inset: Measured CV of $K_{1/2}$ for WT and high variability populations (solid-colored bars), along with predicted CV of $K_{1/2}$ obtained from the mixed-species MWC model using the receptor ratio distributions in Figure 3c as input (dashed-colored bars) and a fixed total number of MWC receptors ($N_{total} = 32$). Error bars indicate 95% confidence intervals obtained through bootstrap resampling. The means are statistically significant different, as determined by a two-sample t-test ($p = 2.9\text{x}10^{-12}$).

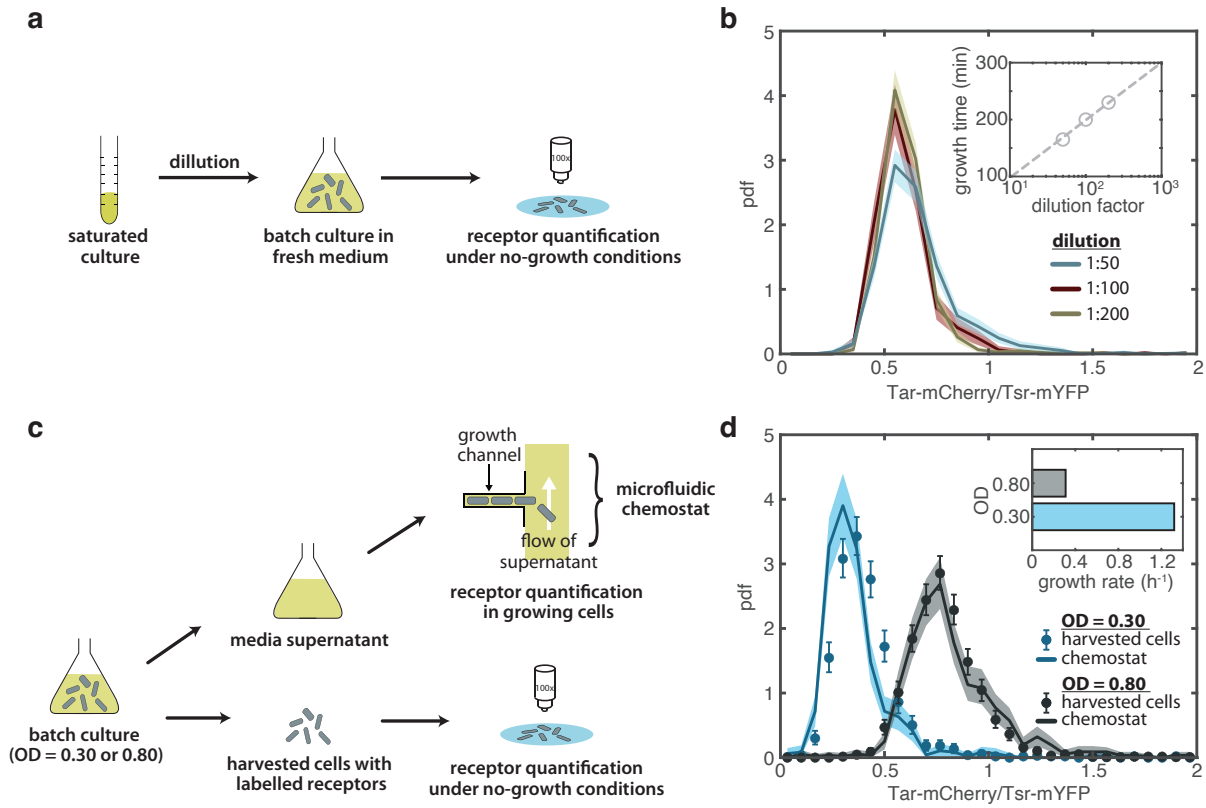

Fig. 4 Growth environment, rather than growth time, determines Tar/Tsr ratio through growth rate-dependent chemoreceptor expression. **(a)** Schematic of the experimental protocol to assess the effect of growth time on the chemoreceptor ratio distributions. Cells from the same saturated culture were diluted to three different concentrations in fresh rich media and all cultures were harvested at the same optical density (OD = 0.45). **(b)** Histograms of the Tar/Tsr chemoreceptor ratio, measured via fluorescence microscopy, for the three different dilutions in a single experiment. The receptor ratio distribution is independent of the dilution factor. Error bars indicate 95% confidence intervals obtained through bootstrap resampling. Inset: Growth time as a function of dilution. **(c)** Schematic of experimental protocol to assess the effect of the growth environment on chemoreceptor ratio distributions. Cells were grown in rich media to OD = 0.30 and OD = 0.80, after which they were separated from their supernatant. The Tar/Tsr chemoreceptor ratio was measured via fluorescence microscopy in both the harvested cells and in cells growing inside a microfluidic chemostat at steady state, where they were exposed to the collected supernatant. **(d)**Histograms of the Tar/Tsr chemoreceptor ratio for harvested cells (solid lines) and for cells growing inside the chemostat while exposed to supernatant (points). Solid lines and points represent the histograms of all measured Tar/Tsr ratios from a single experiment. Shaded areas and error bars indicate 95% confidence intervals obtained through bootstrap resampling. Inset: growth rate of the cells in the batch culture at OD = 0.30 and OD = 0.80, assessed using a plate reader. Bar plots are the means of 40 technical replicates.

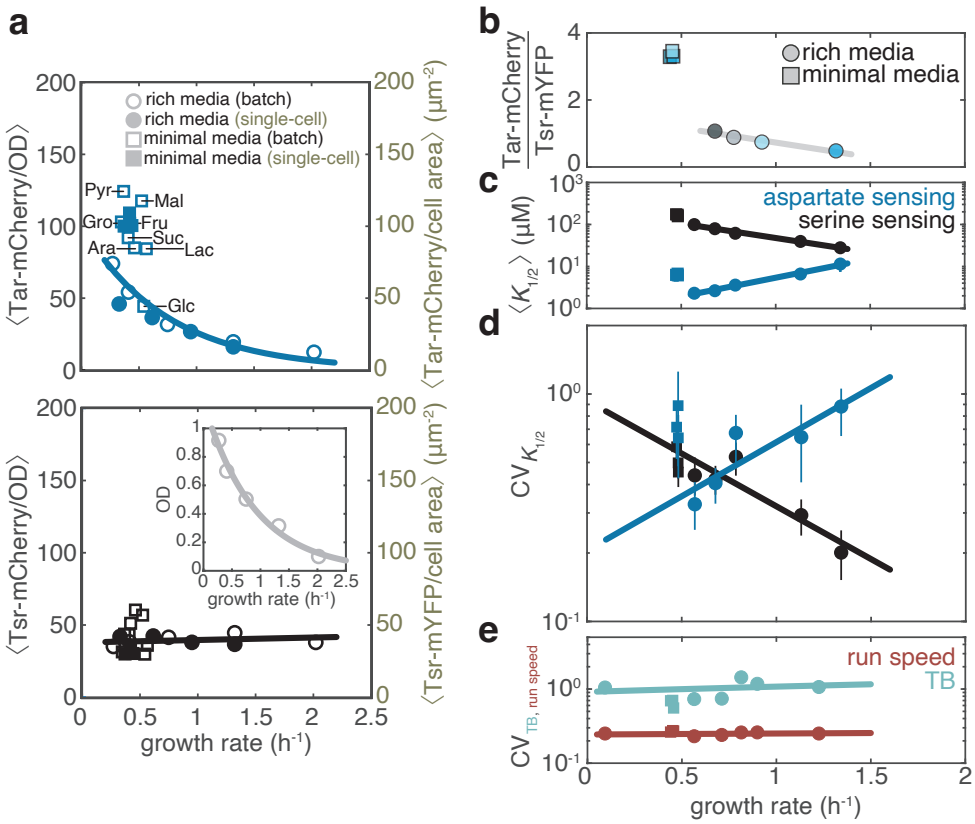

Fig. 5 Bacteria regulate their sensory diversity based on growth rate. **(a)** (Top) Concentration of Tar proteins as a function of growth rate. Protein concentration in batch cultures (hollow points) is defined as the mean fluorescence between two time points during growth divided by the mean biomass (OD) at the same two time points. Carbon sources used to supplement minimal media are indicated as: Gro: 0.5% v/v glycerol; Pyr: 20 mM pyruvate; Fru: 20 mM fructose; Suc: 15 mM succinate; Lac: 20 mM lactose; Ara: 20 mM arabinose; Mal: 20 mM Maltose; and Glc: 0.4% v/v glycose. For all minimal media experiments, expression levels were extracted between OD 0.2 and 0.8, during which growth rate remained approximately constant. Protein concentration is also measured at the single-cell level via fluorescence microscopy (filled points). Filled points represent the means of the Tar concentration distributions shown in EDF 4. Hollow points are the means of 8 technical replicates for each carbon source in minimal media or 40 technical replicates for each OD in rich media. Solid lines are fits to the data. Growth rate, OD, and batch fluorescence levels were assessed in the same batch cultures using a plate reader. (Bottom) Same as the top panel, but for Tsr concentration. Filled points represent the means of the Tsr concentration distributions shown in EDF 4. Inset: growth rate as a function of OD. Points represent growth rates extracted at the same culture phases as expression levels (see methods). **(b)** Scaling of mean Tar/Tsr receptor ratio as a function of growth rate for cells grown in rich (circles) and minimal (squares) media. Same color coding as figure 2c and e. Error bars indicate 95% confidence intervals of the mean $K_{1/2}$ obtained via bootstrap resampling and are typically on the order of the data point size. **(c)** Scaling of mean L-serine (black) and L-aspartate (blue) $K_{1/2}$ as a function of growth rate for cells grown in rich and minimal media. Error bars indicate 95% confidence intervals of the mean $K_{1/2}$ obtained via bootstrap resampling and are typically on the order of the data point size. **(d)** Coefficient of variation (CV) of L-serine (black) and L-aspartate (blue) $K_{1/2}$ as a function of growth rate. Error bars indicate 95% confidence intervals of the CV obtained via bootstrap resampling. **(e)** CV of tumble bias (green) and run speed (brown) as a function of growth rate. Error bars indicate 95% confidence intervals of the CV obtained via bootstrap resampling and are typically on the order of the data point size.

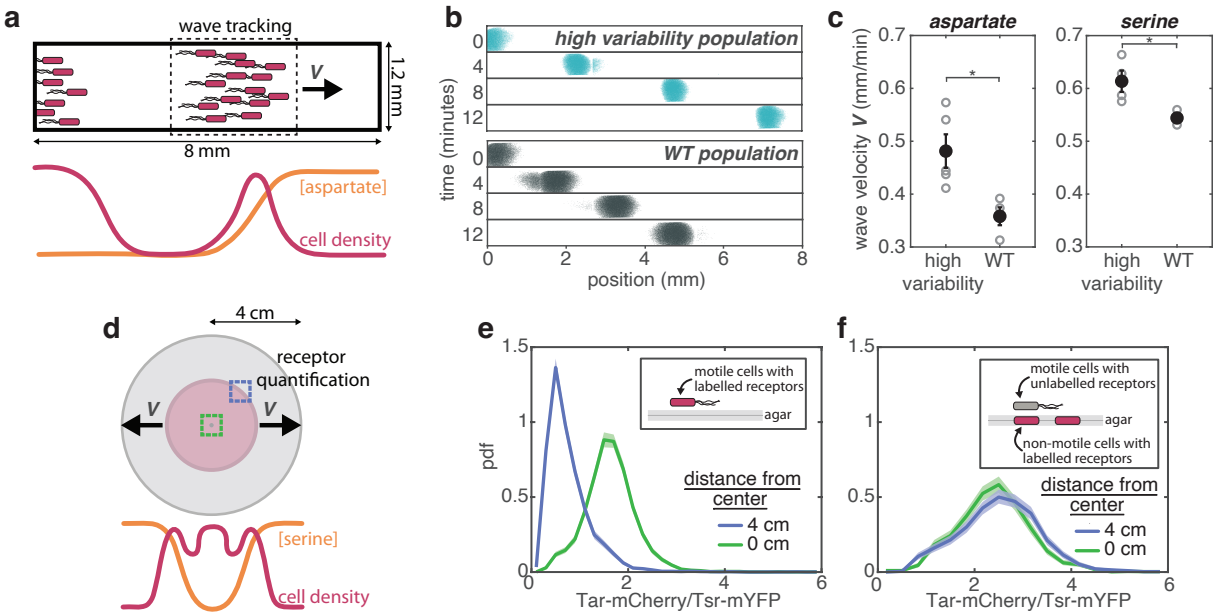

Fig. 6 Sensory diversity enhances the chemotactic migration of isogenic populations across environments through phenotypic filtering **(a)** Schematic of the bacterial speed competition assay. Cells introduced at the entrance of a microfluidic channel form a band that migrates through a self-generated gradient of L-aspartate, established by bacterial consumption. **(b)** Segmented images of bacterial bands formed by a high variability population (top) and a wild-type (WT) population (bottom). Images are from two separate experiments, aligned at time t = 0 for comparison. Refer to Figures 3b and 3c for the Tar/Tsr ratio and $K_{1/2}$ distributions of these two populations, respectively. **(c)** Wave velocities of cells migrating up a 100μM L-aspartate gradient (left) or a 100μM L-serine gradient (right). Hollow points represent independent biological replicates, while solid points indicate the mean values across all replicates. Error bars represent standard error of the mean. Means are statistically significant different, as determined by a two-sample t-test with p = 0.0159 for aspartate waves and p = 0.0385 for the serine waves. **(d)** Schematic of the swim plate assay. Cells on rich media swim plates form a high-density band that migrates up a self-generated L-serine gradient. **(e)** Histograms of the Tar/Tsr chemoreceptor ratio, measured via fluorescence microscopy for motile cells collected from the edge (blue) or center (green) of the expanding colony. **(f)** Same as panel e, but for non-motile cells acting as a biosensor for gene expression collected at the edge (blue) or center (green) of the colony. A motile but unlabeled strain was used to establish the chemical gradient experienced by the biosensor cells. Solid lines represent the histograms of all Tar/Tsr ratios from a single experiment. Shaded areas indicate 95% confidence intervals obtained through bootstrap resampling.

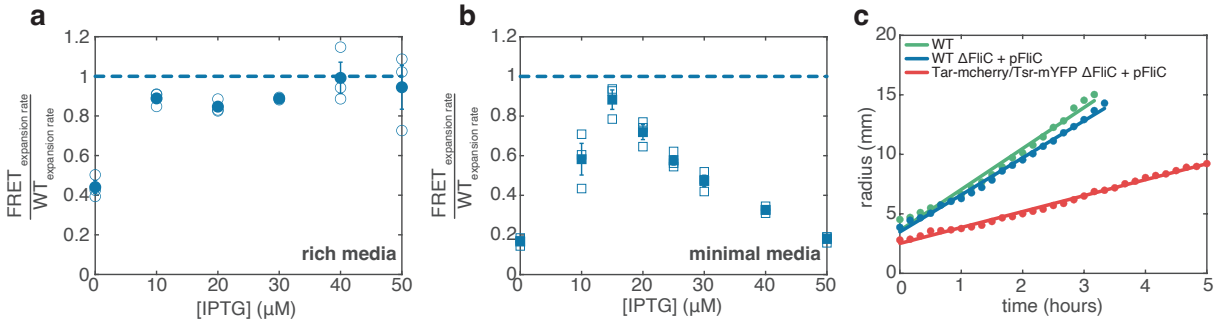

EDF 1 Expansion rate of FRET and receptor-labeled strains. **(a)** Cells expressing CheY and CheZ protein fusions (TSS2114/pSJAB106), used for FRET experiments, yield chemotactic phenotypes with expansion rates nearly identical to WT cells (TSS2096/pTrc99A) when inoculated on rich media soft agar swim plates and induced with 40 or 50 μM IPTG. Hollow symbols represent technical replicates (three for each inducer concentration), while filled symbols represent the mean values of the three replicates. Error bars indicate the standard error of the mean and are typically the size of the graph points. **(b)** Similar to panel a, but for minimal media soft agar swim plates. When induced with 15 μM IPTG, the FRET strain yields an expansion rate nearly identical to that of WT cells. **(c)** Colony expansion of receptor-labeled strain as a function of time. Tar and Tsr protein fusions, used in receptor quantification experiments, produce chemotactic phenotypes when inoculated on rich media soft agar swim plates. Lines represent linear fits to the data points to determine the expansion rates. The expansion rates for the different strains are as follows: 3.23 ± 0.22 mm/hour (WT), 3.10 ± 0.20 mm/hour (WT ΔFliC + pFliC), and 1.28 ± 0.06 mm/hour (Tar-mCherry/Tsr-YFP ΔFliC + pFliC). The abbreviation pFliC denotes pBAD33-based plasmid pC100B-12 expressing WT FliC. WT carries empty pBAD33 (TSS2096/pBAD33), WT ΔFliC + pFliC is strain TSS2097/pC100B-12, and Tar-mCherry/Tsr-YFP ΔFliC + pFliC is strain TSS2144/ pC100B-12. Averages and standard errors of the mean are derived from two technical replicates.

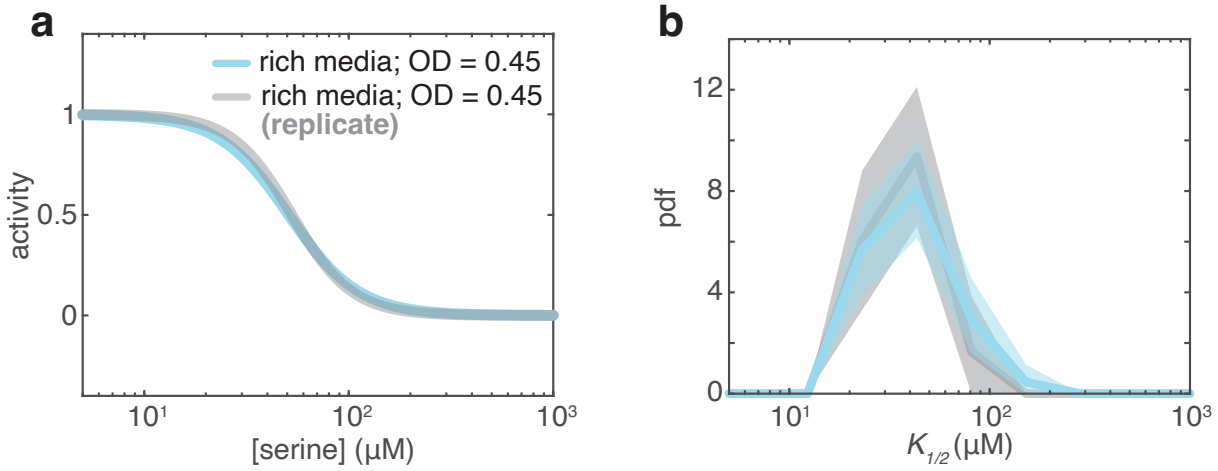

EDF 2 Reproducibility of FRET dose-response experiment. **(a)** Hill function fits to the population-averaged L-serine dose-response data for cells grown to OD = 0.45 in rich media. The blue dose-response curve is replotted from Figure 1b. The gray dose-response curve represents a biological replicate performed on a different day with different ligand dilutions and is identical to the original dose-response curve. **(b)** Histograms of $k_{1/2}$ values obtained from single-cell dose-response curves for cells grown to OD = 0.45 in rich media. The blue distribution is replotted from Figure 1b, and the gray distribution is extracted from single-cell dose-response curves from the same biological replicate as in panel a, showing identical of $k_{1/2}$ distributions. Shaded areas represent 95% confidence intervals obtained through bootstrap resampling of the data.

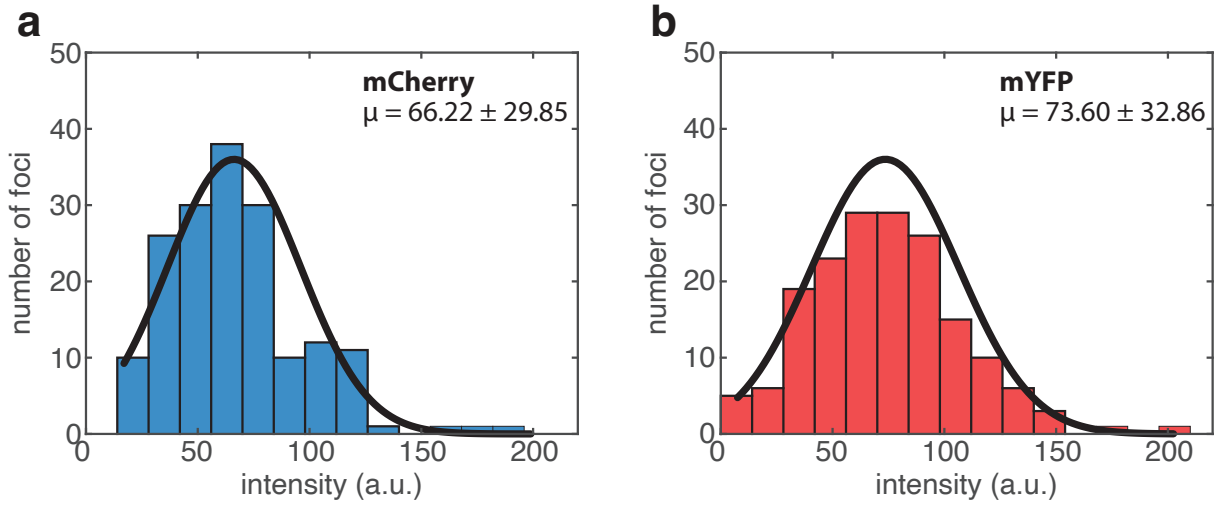

EDF 3 Equating the Tar-mCherry/Tsr-mYFP fluorescence intensity ratio to Tar/Tsr receptor abundance ratio. A chemically fixed FROS strain containing six mCherry- and mYFP-repressor fusions on its chromosome (panels **a** and **b**, respectively) was imaged using the same settings and optical path as used in receptor-labeled experiments. The mean measured mCherry/YFP fluorescence intensity ratio (μ denotes mean value $\pm$ standard deviation) was close to unity, indicating that the Tar-mCherry/Tsr-mYFP fluorescence intensity ratio effectively reflects the Tar/Tsr receptor abundance ratio.

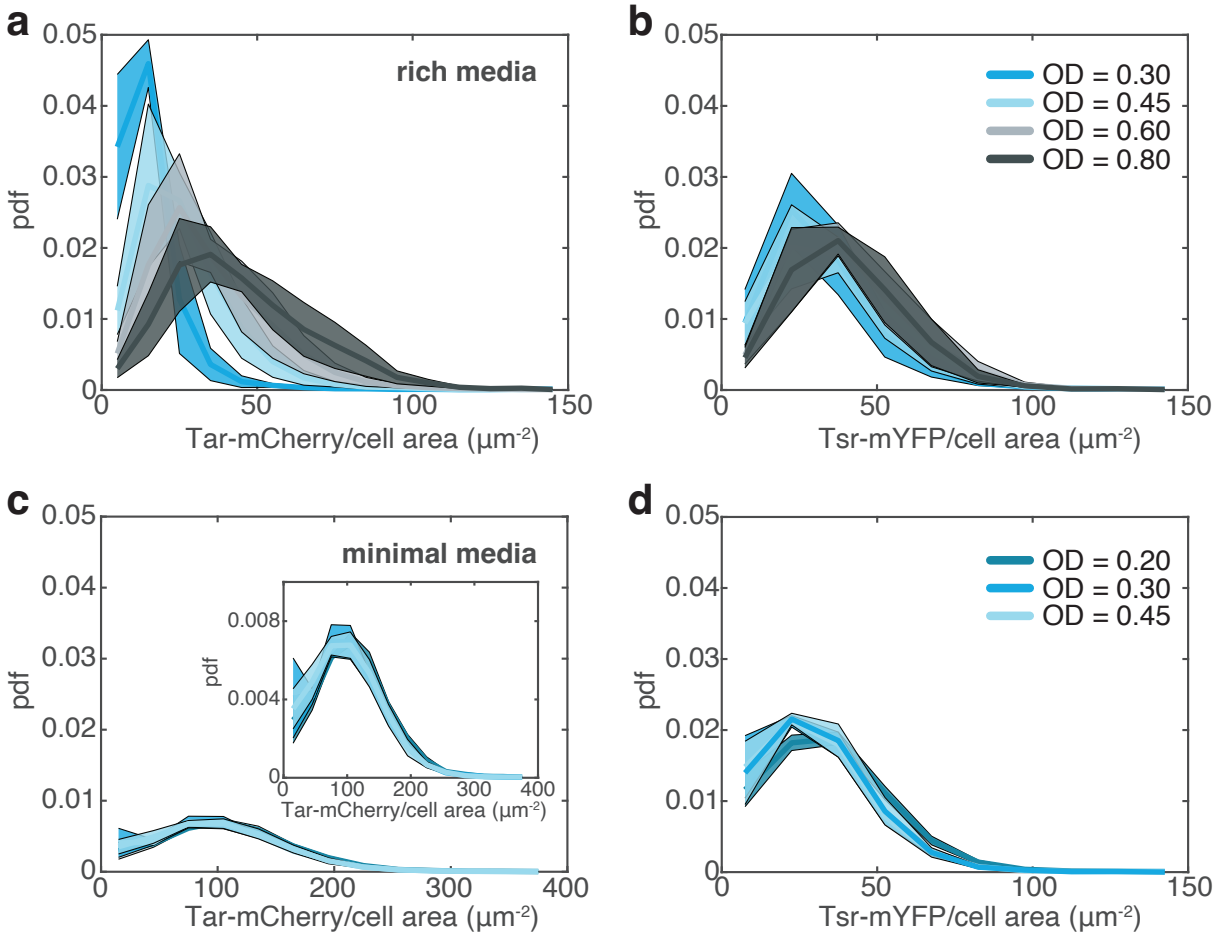

EDF 4 Tar and Tsr chemoreceptor expression under different growth conditions. **(a)** Histograms of Tar-mCherry expression measured with fluorescence microscopy for cells grown to different optical densities (ODs) in rich media. Solid lines represent the mean of four independent biological replicates, with shaded areas indicating the standard error of the mean. The Figure legend and color scheme match panel b. **(b)** Same as panel a, but for Tsr-mYFP. **(c)** Histograms of Tar-mCherry expression for cells grown to different ODs in minimal media. Solid lines represent the mean of three independent biological replicates, with shaded areas indicating the standard error of the mean. The Figure legend and color scheme match panel d. Inset: magnified version of the plot. **(d)** Same as panel c, but for Tsr-mYFP.

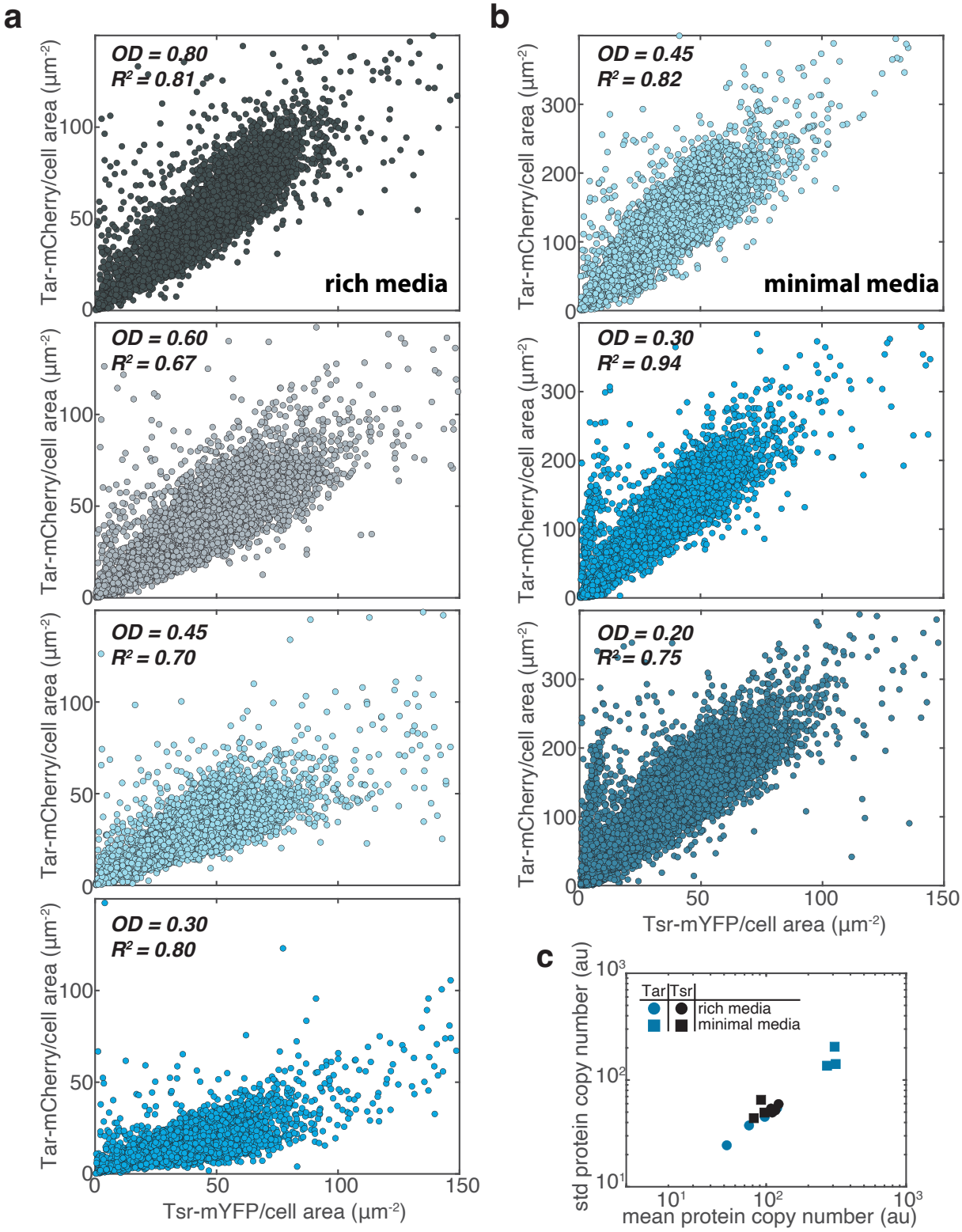

EDF 5 Tar and Tsr chemoreceptor expression is corelated under all growth conditions. **(a)** Correlation between Tar-mCherry and Tsr-mYFP expression for cells grown to different optical densities (ODs) in rich media, measured using fluorescence microscopy. Each point represents a single cell, derived from four independent biological replicates. **(b)** Similar to panel a, but for cells grown in minimal media, with points obtained from three independent biological replicates. **(c)** Scaling of the mean and standard deviation of protein copy numbers (in arbitrary units) for Tar and Tsr across all conditions.

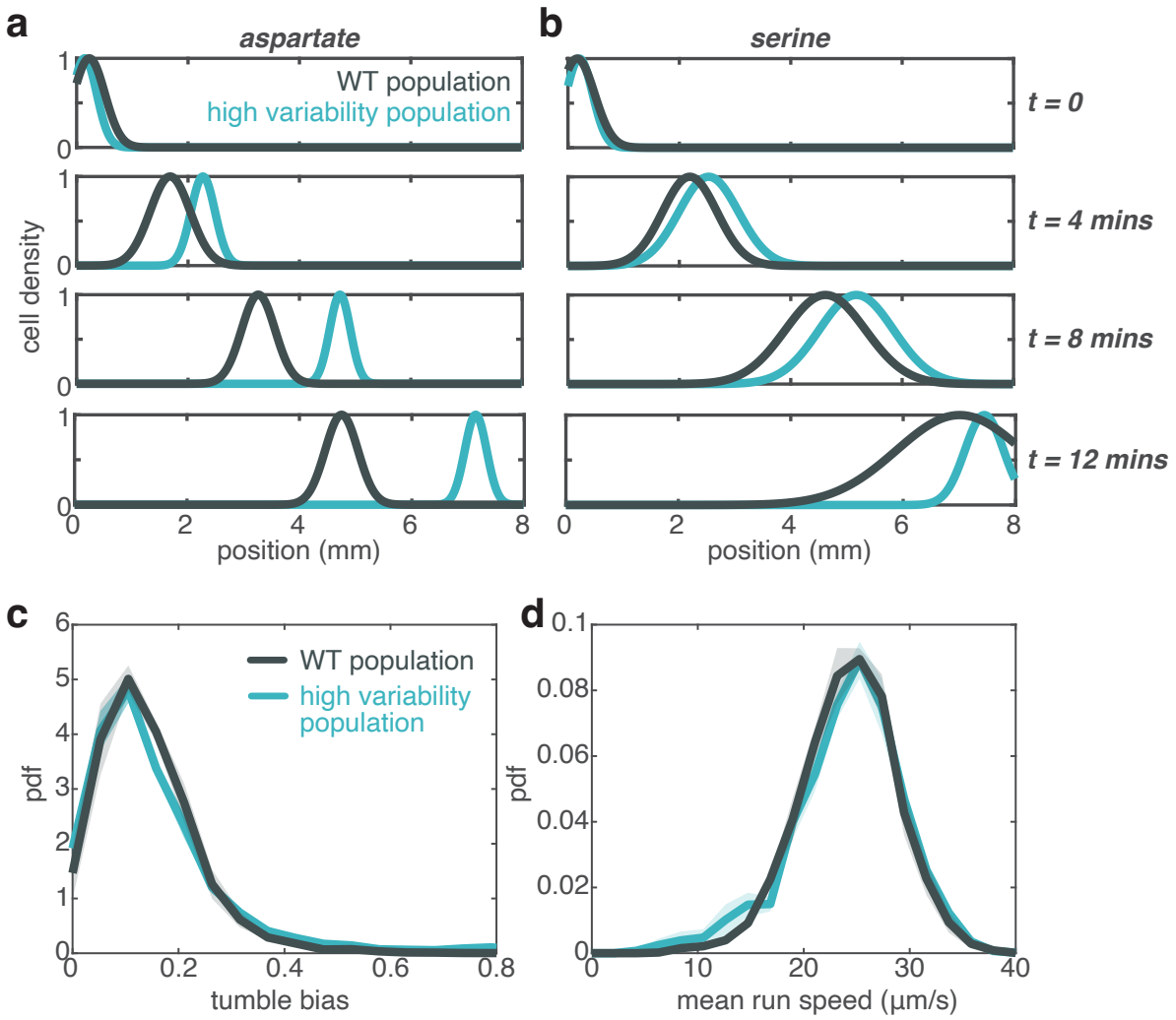

EDF 6 Wave position, tumble bias, and run speed distributions of the WT and high variability populations. . **(a)** Wave position of the high variability (left) and wild-type (WT) population (right) in a gradient of 100 μM L-aspartate. Cell density is extracted from the segmented wave images shown on figure 6b. Curves represent Gaussian function fits to the images. **(b)** Similar to panel a, but for cells in a gradient of 100 μM L-serine. **(c)** Tumble bias distribution of the high variability and wild-type populations in the absence of a chemical gradient are identical. Solid lines represent the mean of four independent biological replicates, with shaded areas indicating the standard error of the mean. **(d)** Same as panel a, but for the mean run speed of the high variability and wild-type populations.

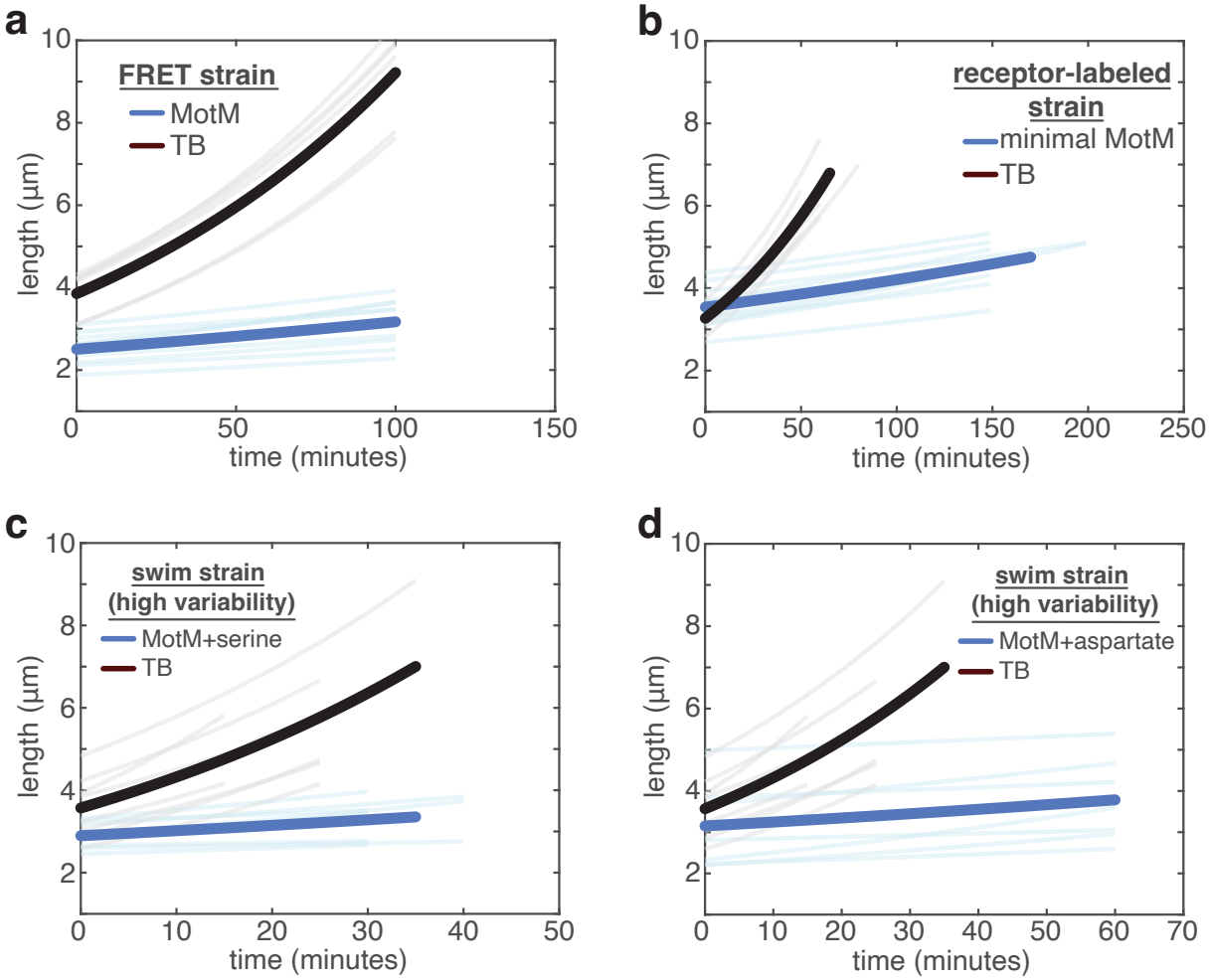

EDF 7 Growth rate of the strains used in this study is negligible during experiments. **(a)** Cell elongation of the FRET strain (TSS2191/pSJAB106) as a function of time. Blue line represents the mean elongation rate of the stain in motility media (MotM), the buffer used for FRET experiments, while the black line represents the mean elongation rate of the same strain in TB, the rich media used to grow the strain. **(b)** Similar to panel a, but for the strain used in receptor-quantification experiments (TSS2155) in its measurement buffer, minimal motility media (minimal MotM). **(c)** Similar to panel a, but for the high variability strain used in swimming competition experiments (TSS2096/pTrc99A/pVS118) in MotM with 100 μM L-serine added. **(d)** Same as in panel c, but with 100 μM L-aspartate added to MotM.

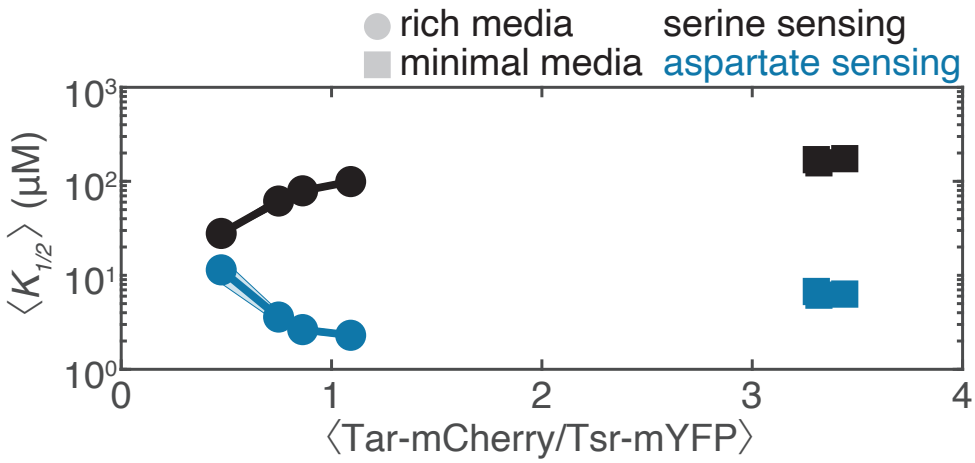

EDF 8 $K_{1/2}$ depends on Tar/Tsr expression ratio. Scaling of L-serine and L-aspartate $K_{1/2}$ as a function of receptor ratio. Scaling of mean L-serine (black) and L-aspartate (blue) $K_{1/2}$ as a function of mean receptor ratio for cells grown in rich (circles) and minimal media (squares). $K_{1/2}$ and receptor ratio were determined in separate experiments with cells grown under identical conditions. Shaded areas indicate 95% confidence intervals of the mean $K_{1/2}$ obtained via bootstrap resampling.

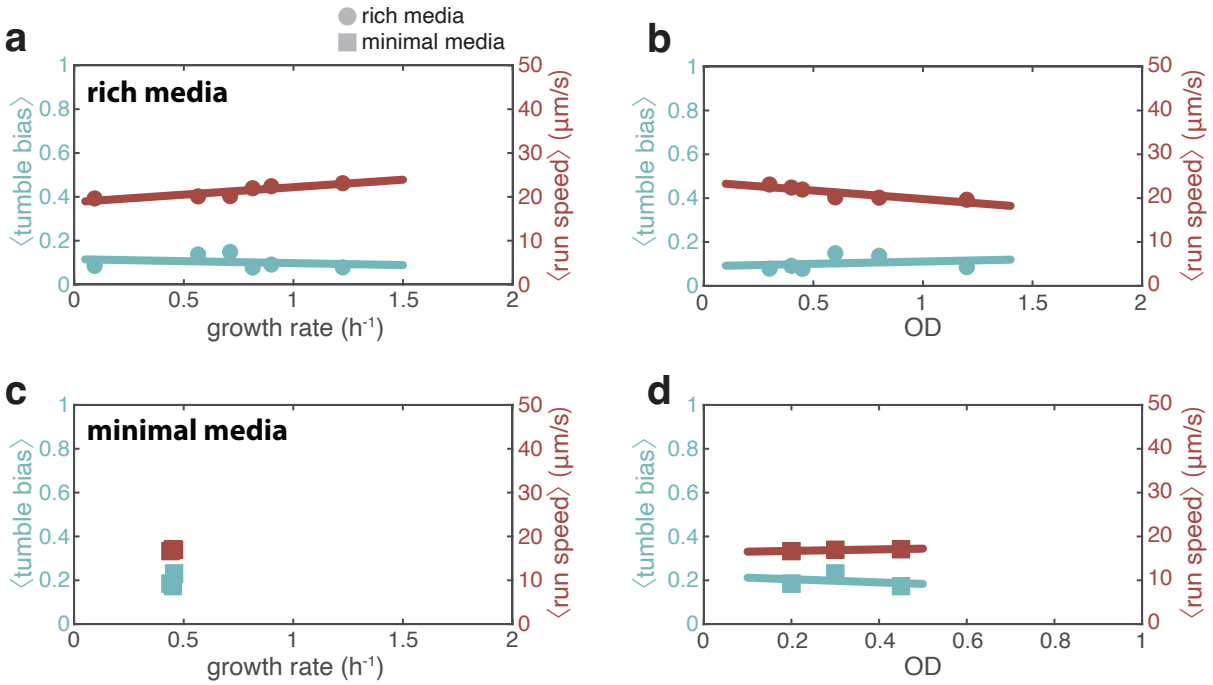

EDF 9 Mean tumble bias and run speed as a function of growth rate and optical density. **(a)** Mean tumble bias and run speed of WT MG1655 as a function of growth rate for cells grown in rich media. Data from a single experiment. Lines are linear fits to the data. **(b)** Same data as panel (a) but plotted against the optical density (OD) of the culture. **(c)** Mean tumble bias and run speed of WT MG1655 as a function of growth rate for cells grown in minimal media. Data from a single experiment. **(d)** Same data as panel (c) but plotted against the optical density (OD) of the culture. Lines are linear fits to the data.

References

[1] Keegstra, J.M., Carrara, F., Stocker, R.: The ecological roles of bacterial chemotaxis. Nature Reviews Microbiology **20**(8), 491–504 (2022) https://doi.org/10.1038/s41579-022-00709-w

[2] Ackermann, M.: A functional perspective on phenotypic heterogeneity in microorganisms. Nature Reviews Microbiology **13**(8), 497–508 (2015) https://doi.org/10.1038/nrmicro3491

[3] Xue, B., Sartori, P., Leibler, S.: Environment-to-phenotype mapping and adaptation strategies in varying environments. Proceedings of the National Academy of Sciences **116**(28), 13847–13855 (2019) https://doi.org/10.1073/pnas.1903232116

[4] Carey, J.N., Mettert, E.L., Roggiani, M., Myers, K.S., Kiley, P.J., Goulian, M.: Regulated Stochasticity in a Bacterial Signaling Network Permits Tolerance to a Rapid Environmental Change. Cell **173**(1), 196–20714 (2018) https://doi.org/10.1016/j.cell.2018.02.005

[5] Schreiber, F., Littmann, S., Lavik, G., Escrig, S., Meibom, A., Kuypers, M.M.M., Ackermann, M.: Phenotypic heterogeneity driven by nutrient limitation promotes growth in fluctuating environments. Nature Microbiology **1**(6), 16055 (2016) https://doi.org/10.1038/nmicrobiol.2016.55

[6] Frankel, N.W., Pontius, W., Dufour, Y.S., Long, J., Hernandez-Nunez, L., Emonet, T.: Adaptability of non-genetic diversity in bacterial chemotaxis. eLife **3**, 03526 (2014) https://doi.org/10.7554/eLife.03526

[7] Waite, A.J., Frankel, N.W., Emonet, T.: Behavioral Variability and Phenotypic Diversity in Bacterial Chemotaxis. Annual Review of Biophysics **47**(1), 595–616 (2018) https://doi.org/10.1146/annurev-biophys-062215-010954

[8] Moore, J.P., Kamino, K., Kottou, R., Shimizu, T.S., Emonet, T.: Signal integration and adaptive sensory diversity tuning in Escherichia coli chemotaxis. Cell Systems **15**(7), 628–6388 (2024) https://doi.org/10.1016/j.cels.2024.06.003

[9] Miller, M.B., Bassler, B.L.: Quorum sensing in bacteria. Annual Reviews in Microbiology **55**(1), 165–199 (2001)

[10] Pai, A., You, L.: Optimal tuning of bacterial sensing potential. Molecular systems biology **5**(1), 286 (2009)

[11] Flemming, H.-C., Wingender, J.: The biofilm matrix. Nature reviews microbiology **8**(9), 623–633 (2010)

[12] Nadell, C.D., Foster, K.R., Xavier, J.B.: Emergence of spatial structure in cell groups and the evolution of cooperation. PLoS computational biology **6**(3), 1000716 (2010)

[13] Lee, H.H., Molla, M.N., Cantor, C.R., Collins, J.J.: Bacterial charity work leads to population-wide resistance. Nature **467**(7311), 82–85 (2010)

[14] Yurtsev, E.A., Chao, H.X., Datta, M.S., Artemova, T., Gore, J.: Bacterial cheating drives the population dynamics of cooperative antibiotic resistance plasmids. Molecular systems biology **9**(1), 683 (2013)

[15] Srinivasan, S., Vladescu, I.D., Koehler, S.A., Wang, X., Mani, M., Rubinstein, S.M.: Matrix production and sporulation in bacillus subtilis biofilms localize to propagating wave fronts. Biophysical Journal **114**(6), 1490–1498 (2018)

[16] Chou, K.-T., Dong-yeon, D.L., Chiou, J.-g., Galera-Laporta, L., Ly, S., Garcia-Ojalvo, J., Süel, G.M.:

A segmentation clock patterns cellular differentiation in a bacterial biofilm. Cell **185**(1), 145–157 (2022)

[17] Kaiser, D.: Coupling cell movement to multicellular development in myxobacteria. Nature Reviews Microbiology **1**(1), 45–54 (2003)

[18] Saulnier, J.-B., Romanos, M., Schrohe, J., Cuzin, C., Calvez, V., Mignot, T.: The mechanism of spatial pattern transition in motile bacterial collectives. bioRxiv, 2024–10 (2024)

[19] Rutherford, S.T., Bassler, B.L.: Bacterial quorum sensing: its role in virulence and possibilities for its control. Cold Spring Harbor perspectives in medicine **2**(11), 012427 (2012)

[20] Cornforth, D.M., Foster, K.R.: Competition sensing: the social side of bacterial stress responses. Nature Reviews Microbiology **11**(4), 285–293 (2013)

[21] Fu, X., Kato, S., Long, J., Mattingly, H.H., He, C., Vural, D.C., Zucker, S.W., Emonet, T.: Spatial self-organization resolves conflicts between individuality and collective migration. Nature Communications **9**(1), 2177 (2018) https://doi.org/10.1038/s41467-018-04539-4

[22] Cremer, J., Honda, T., Tang, Y., Wong-Ng, J., Vergassola, M., Hwa, T.: Chemotaxis as a navigation strategy to boost range expansion. Nature **575**(7784), 658–663 (2019) https://doi.org/10.1038/s41586-019-1733-y

[23] Gude, S., Pinçe, E., Taute, K.M., Seinen, A.-B., Shimizu, T.S., Tans, S.J.: Bacterial coexistence driven by motility and spatial competition. Nature **578**(7796), 588–592 (2020) https://doi.org/10.1038/s41586-020-2033-2

[24] Spudich, J.L., Koshland, D.E.: Non-genetic individuality: chance in the single cell. Nature **262**(5568), 467–471 (1976) https://doi.org/10.1038/262467a0

[25] Kollmann, M., Løvdok, L., Bartholomé, K., Timmer, J., Sourjik, V.: Design principles of a bacterial signalling network. Nature **438**(7067), 504–507 (2005) https://doi.org/10.1038/nature04228

[26] Park, H., Pontius, W., Guet, C.C., Marko, J.F., Emonet, T., Cluzel, P.: Interdependence of behavioural variability and response to small stimuli in bacteria. Nature **468**(7325), 819–823 (2010) https://doi.org/10.1038/nature09551

[27] Keegstra, J.M., Kamino, K., Anquez, F., Lazova, M.D., Emonet, T., Shimizu, T.S.: Phenotypic diversity and temporal variability in a bacterial signaling network revealed by single-cell FRET. eLife **6**, 27455 (2017) https://doi.org/10.7554/eLife.27455

[28] Waite, A.J., Frankel, N.W., Dufour, Y.S., Johnston, J.F., Long, J., Emonet, T.: Non-genetic diversity modulates population performance. Molecular Systems Biology **12**(12), 895 (2016) https://doi.org/10.15252/msb.20167044

[29] Dufour, Y.S., Fu, X., Hernandez-Nunez, L., Emonet, T.: Limits of Feedback Control in Bacterial Chemotaxis. PLoS Computational Biology **10**(6), 1003694 (2014) https://doi.org/10.1371/journal.pcbi.1003694

[30] Salek, M.M., Carrara, F., Fernandez, V., Guasto, J.S., Stocker, R.: Bacterial chemotaxis in a microfluidic T-maze reveals strong phenotypic heterogeneity in chemotactic sensitivity. Nature Communications **10**(1), 1877 (2019) https://doi.org/10.1038/s41467-019-09521-2

[31] Kamino, K., Keegstra, J.M., Long, J., Emonet, T., Shimizu, T.S.: Adaptive tuning of cell sensory diversity without changes in gene expression. Science Advances **6**(46), 1087 (2020) https://doi.org/10.1126/sciadv.abc1087

[32] Parkinson, J.S., Hazelbauer, G.L., Falke, J.J.: Signaling and sensory adaptation in Escherichia coli chemoreceptors: 2015 update. Trends in Microbiology **23**(5), 257–266 (2015) https://doi.org/10.1016/j.tim.2015.03.003

[33] Li, M., Hazelbauer, G.L.: Cellular Stoichiometry of the Components of the Chemotaxis Signaling Complex. Journal of Bacteriology **186**(12), 3687–3694 (2004) https://doi.org/10.1128/JB.186.12.3687-3694.2004

[34] Vo, L., Avgidis, F., Mattingly, H.H., Edmonds, K., Burger, I., Balasubramanian, R., Shimizu, T.S., Kazmierczak, B.I., Emonet, T.: Nongenetic adaptation by collective migration. Proceedings of the National Academy of Sciences **122**(8), 2423774122 (2025) https://doi.org/10.1073/pnas.2423774122

[35] Monod, J., Wyman, J., Changeux, J.-P.: On the nature of allosteric transitions: A plausible model (1965)

[36] Mello, B.A., Tu, Y.: An allosteric model for heterogeneous receptor complexes: Understanding bacterial chemotaxis responses to multiple stimuli. Proceedings of the National Academy of Sciences **102**(48), 17354–17359 (2005) https://doi.org/10.1073/pnas.0506961102

[37] Wang, P., Robert, L., Pelletier, J., Dang, W.L., Taddei, F., Wright, A., Jun, S.: Robust Growth of Escherichia coli. Current Biology **20**(12), 1099–1103 (2010) https://doi.org/10.1016/j.cub.2010.04.045

[38] Mattingly, H.H., Emonet, T.: Collective behavior and nongenetic inheritance allow bacterial populations to adapt to changing environments. Proceedings of the National Academy of Sciences **119**(26), 2117377119 (2022) https://doi.org/10.1073/pnas.2117377119

[39] Yang, Y., M. Pollard, A., Höfler, C., Poschet, G., Wirtz, M., Hell, R., Sourjik, V.: Relation between chemotaxis and consumption of amino acids in bacteria. Molecular Microbiology **96**(6), 1272–1282 (2015) https://doi.org/10.1111/mmi.13006

[40] Prüss, B.M., Nelms, J.M., Park, C., Wolfe, A.J.: Mutations in NADH:ubiquinone oxidoreductase of Escherichia coli affect growth on mixed amino acids. Journal of Bacteriology **176**(8), 2143–2150 (1994) https://doi.org/10.1128/jb.176.8.2143-2150.1994

[41] Selvarasu, S., Ow, D.S., Lee, S.Y., Lee, M.M., Oh, S.K., Karimi, I.A., Lee, D.: Characterizing *Escherichia coli* DH5 growth and metabolism in a complex medium using genome-scale flux analysis. Biotechnology and Bioengineering **102**(3), 923–934 (2009) https://doi.org/10.1002/bit.22119

[42] Adler, J., Hazelbauer, G.L., Dahl, M.M.: Chemotaxis Toward Sugars in *Escherichia coli*. Journal of Bacteriology **115**(3), 824–847 (1973) https://doi.org/10.1128/jb.115.3.824-847.1973

[43] Taniguchi, Y., Choi, P.J., Li, G.-W., Chen, H., Babu, M., Hearn, J., Emili, A., Xie, X.S.: Quantifying *E. coli* Proteome and Transcriptome with Single-Molecule Sensitivity in Single Cells. Science **329**(5991), 533–538 (2010) https://doi.org/10.1126/science.1188308

[44] Kalinin, Y., Neumann, S., Sourjik, V., Wu, M.: Responses of *Escherichia coli* Bacteria to Two Opposing Chemoattractant Gradients Depend on the Chemoreceptor Ratio. Journal of Bacteriology **192**(7), 1796–1800 (2010) https://doi.org/10.1128/JB.01507-09

[45] Li, L., Zhang, X., Sun, Y., Ouyang, Q., Tu, Y., Luo, C.: Phenotypic Variability Shapes Bacterial Responses to Opposing Gradients. PRX Life **2**(1), 013001 (2024) https://doi.org/10.1103/PRXLife.2.013001

[46] Yoney, A., Salman, H.: Precision and Variability in Bacterial Temperature Sensing. Biophysical Journal **108**(10), 2427–2436 (2015) https://doi.org/10.1016/j.bpj.2015.04.016

[47] Salman, H., Libchaber, A.: A concentration-dependent switch in the bacterial response to temperature. Nature Cell Biology **9**(9), 1098–1100 (2007) https://doi.org/10.1038/ncb1632

[48] Yang, Y., Sourjik, V.: Opposite responses by different chemoreceptors set a tunable preference point in *E scherichia coli* pH taxis. Molecular Microbiology **86**(6), 1482–1489 (2012) https://doi.org/10.1111/mmi.12070

[49] Chilcott, G.S., Hughes, K.T.: Coupling of Flagellar Gene Expression to Flagellar Assembly in *Salmonella enterica* Serovar Typhimurium and *Escherichia coli*. Microbiology and Molecular Biology Reviews **64**(4), 694–708 (2000) https://doi.org/10.1128/MMBR.64.4.694-708.2000

[50] Elowitz, M.B., Levine, A.J., Siggia, E.D., Swain, P.S.: Stochastic Gene Expression in a Single Cell. Science **297**(5584), 1183–1186 (2002) https://doi.org/10.1126/science.1070919

[51] Balakrishnan, R., Mori, M., Segota, I., Zhang, Z., Aebersold, R., Ludwig, C., Hwa, T.: Principles of gene regulation quantitatively connect DNA to RNA and proteins in bacteria. Science **378**(6624), 2066 (2022) https://doi.org/10.1126/science.abk2066

[52] Ames, P., Studdert, C.A., Reiser, R.H., Parkinson, J.S.: Collaborative signaling by mixed chemoreceptor teams in *Escherichia coli*. Proceedings of the National Academy of Sciences **99**(10), 7060–7065 (2002) https://doi.org/10.1073/pnas.092071899

[53] Ni, B., Colin, R., Link, H., Endres, R.G., Sourjik, V.: Growth-rate dependent resource investment in bacterial motile behavior quantitatively follows potential benefit of chemotaxis. Proceedings of the National Academy of Sciences **117**(1), 595–601 (2020) https://doi.org/10.1073/pnas.1910849117

[54] Khursigara, C.M., Lan, G., Neumann, S., Wu, X., Ravindran, S., Borgnia, M.J., Sourjik, V., Milne, J., Tu, Y., Subramaniam, S.: Lateral density of receptor arrays in the membrane plane influences sensitivity of the E. coli chemotaxis response. The EMBO Journal **30**(9), 1719–1729 (2011) https://doi.org/10.1038/emboj.2011.77

[55] Honda, T., Cremer, J., Mancini, L., Zhang, Z., Pilizota, T., Hwa, T.: Coordination of gene expression with cell size enables *Escherichia coli* to efficiently maintain motility across conditions. Proceedings of the National Academy of Sciences **119**(37), 2110342119 (2022) https://doi.org/10.1073/pnas.2110342119

[56] Staropoli, J.F., Alon, U.: Computerized Analysis of Chemotaxis at Different Stages of Bacterial Growth. Biophysical Journal **78**(1), 513–519 (2000) https://doi.org/10.1016/S0006-3495(00)76613-6

[57] Phan, T.V., Mattingly, H.H., Vo, L., Marvin, J.S., Looger, L.L., Emonet, T.: Direct measurement of dynamic attractant gradients reveals breakdown of the Patlak–Keller–Segel chemotaxis model. Proceedings of the National Academy of Sciences **121**(3), 2309251121 (2024) https://doi.org/10.1073/pnas.2309251121

[58] Bai, Y., He, C., Chu, P., Long, J., Li, X., Fu, X.: Spatial modulation of individual behaviors enables an ordered structure of diverse phenotypes during bacterial group migration. eLife **10**, 67316 (2021) https://doi.org/10.7554/eLife.67316

[59] Wong-Ng, J., Melbinger, A., Celani, A., Vergassola, M.: The Role of Adaptation in Bacterial Speed Races. PLOS Computational Biology **12**(6), 1004974 (2016) https://doi.org/10.1371/journal.pcbi.1004974

[60] Wolfe, A.J., Berg, H.C.: Migration of bacteria in semisolid agar. Proceedings of the National Academy of Sciences **86**(18), 6973–6977 (1989) https://doi.org/10.1073/pnas.86.18.6973

[61] Hobby, G.L., Meyer, K., Chaffee, E.: Observations on the mechanism of action of penicillin. Proceedings of the Society for Experimental Biology and Medicine **50**(2), 281–285 (1942)

[62] Bigger, J.: Treatment of staphyloeoeeal infections with penicillin by intermittent sterilisation. (1944)

[63] Balaban, N.Q., Merrin, J., Chait, R., Kowalik, L., Leibler, S.: Bacterial Persistence as a Phenotypic Switch. Science **305**(5690), 1622–1625 (2004) https://doi.org/10.1126/science.1099390

[64] Kussell, E., Leibler, S.: Phenotypic Diversity, Population Growth, and Information in Fluctuating Environments. Science **309**(5743), 2075–2078 (2005) https://doi.org/10.1126/science.1114383

[65] Veening, J.-W., Stewart, E.J., Berngruber, T.W., Taddei, F., Kuipers, O.P., Hamoen, L.W.: Bet-hedging and epigenetic inheritance in bacterial cell development. Proceedings of the National Academy of Sciences **105**(11), 4393–4398 (2008) https://doi.org/10.1073/pnas.0700463105

[66] Dufour, Y.S., Gillet, S., Frankel, N.W., Weibel, D.B., Emonet, T.: Direct Correlation between Motile Behavior and Protein Abundance in Single Cells. PLOS Computational Biology **12**(9), 1005041 (2016) https://doi.org/10.1371/journal.pcbi.1005041

[67] Løvdok, L., Bentele, K., Vladimirov, N., Müller, A., Pop, F.S., Lebiedz, D., Kollmann, M., Sourjik, V.: Role of Translational Coupling in Robustness of Bacterial Chemotaxis Pathway. PLoS Biology **7**(8), 1000171 (2009) https://doi.org/10.1371/journal.pbio.1000171

[68] Lisevich, I., Colin, R., Yang, H.Y., Ni, B., Sourjik, V.: Physics of swimming and its fitness cost determine strategies of bacterial investment in flagellar motility. Nature Communications **16**(1), 1731 (2025) https://doi.org/10.1038/s41467-025-56980-x

[69] Si, G., Wu, T., Ouyang, Q., Tu, Y.: Pathway-based mean-field model for escherichia coli chemotaxis. Physical review letters **109**(4), 048101 (2012)

[70] Vo, L., Avgidis, F., Mattingly, H.H., Balasubramanian, R., Shimizu, T.S., Kazmierczak, B.I., Emonet, T.: Non-genetic adaptation by collective migration (2024). https://doi.org/10.1101/2024.01.02.573956 . http://biorxiv.org/lookup/doi/10.1101/2024.01.02.573956

[71] Interactions and self-organization in the soil-microbe complex. Science **304**(5677), 1634–1637 (2004)

[72] Donaldson, G.P., Lee, S.M., Mazmanian, S.K.: Gut biogeography of the bacterial microbiota. Nature Reviews Microbiology **14**(1), 20–32 (2016)

[73] Spatial Organization of the Bacterial Cell: in Vivo Imaging Across Scales. publisher not identified, The Netherlands (2019). OCLC: 1088406919

[74] Keegstra, J.M., Avgidis, F., Mulla, Y., Parkinson, J.S., Shimizu, T.S.: Near-critical tuning of cooperativity revealed by spontaneous switching in a protein signalling array (2022). https://doi.org/10.1101/2022.12.04.518992 . http://biorxiv.org/lookup/doi/10.1101/2022.12.04.518992

[75] Qin, D., Xia, Y., Whitesides, G.M.: Soft lithography for micro- and nanoscale patterning. Nature Protocols **5**(3), 491–502 (2010) https://doi.org/10.1038/nprot.2009.234

[76] Kim, J.M., Garcia-Alcala, M., Balleza, E., Cluzel, P.: Stochastic transcriptional pulses orchestrate flagellar biosynthesis in *Escherichia coli*. Science Advances **6**(6), 0947 (2020) https://doi.org/10.1126/sciadv.aax0947

[77] Ronneberger, O., Fischer, P., Brox, T.: U-Net: Convolutional Networks for Biomedical Image Segmentation. arXiv. arXiv:1505.04597 [cs] (2015). http://arxiv.org/abs/1505.04597

[78] Kamino, K., Kadakia, N., Avgidis, F., Liu, Z.-X., Aoki, K., Shimizu, T., Emonet, T.: Optimal inference of molecular interaction dynamics in FRET microscopy. Proceedings of the National Academy of Sciences **120**(15), 2211807120 (2023) https://doi.org/10.1073/pnas.2211807120

[79] Kamande, J.W., Wang, Y., Taylor, A.M.: Cloning SU8 silicon masters using epoxy resins to increase feature replicability and production for cell culture devices. Biomicrofluidics **9**(3), 036502 (2015) https://doi.org/10.1063/1.4922962

[80] Mattingly, H.H., Kamino, K., Machta, B.B., Emonet, T.: Escherichia coli chemotaxis is information limited. Nature Physics **17**(12), 1426–1431 (2021) https://doi.org/10.1038/s41567-021-01380-3